Simulation and Design of Infrared Second-Order Nonlinear Optical Materials in Metal Cluster Compounds

Kechen Wu

Abstract In this minireview, we overview the recent advances and perspectives in the developments of the infrared second-order nonlinear optical materials. The traditional semiconductors are discussed first including the problems encountered such as the facility of large second-order nonlinearity but difficulty in practical materials for laser applications. We then focus our special interest on the area of the transition-metal polynuclear cluster compounds which is a great promising area for developing new-generation infrared second-order nonlinear optical materials and molecule-scaled photoelectronic devices. We present in detail the computational studies on the microscopic mechanism of second-order nonlinear optical response and the structure–property relationship insight of these metal cluster compounds.

Keywords Charge transfers · Density functional calculations · IR absorption · Nonlinear optics · Transition-metal compounds

Contents

K. Wu (✉)
State Key Laboratory of Structural Chemistry, Fujian Institute of Research on the Structure of Matter, Chinese Academy of Sciences, Fuzhou 350002, People's Republic of China
e-mail: wkc@fjirsm.ac.cn

1   Introduction of IR NLO Materials

The infrared (IR) optical crystalline material is optically transparent in the IR region (0.7–400 μm), i.e., it is not absorbed or less absorbed by the light in this specified spectroscopic region. In fact, most of the materials applied in the IR region cannot be transparent through the whole IR region. The materials that have one or more applicable transparent windows are named as IR optical materials specified in their transparency windows. The linear optical (LO) modulations of the IR optical materials such as propagation, reflection, refraction, diffraction, etc., have been widely applied in the areas of meteorological monitoring, remote sensing, laser distance measuring, missile guidance, and laser communication. The IR optical material with the large nonlinear optical (NLO) response (so-called IR NLO material) could perform NLO modulations to light, especially laser light, in the IR region. It can nonlinearly modulate the laser frequency like frequency doubling, frequency converting, and frequency oscillating [1]. At present, the laser-pumped radiations in the IR region are less than those in the UV-vis region (1.064 μm radiation pumped by Nd-YAG laser in the near-IR region and 10.6 μm pumped by CO_2 gas laser in the mid-IR region are two typical ones). The applicable IR NLO materials can effectively widen the IR laser radiations so that they can greatly improve the applications of laser devices in the long-wavelength space. The most demanded example is long-distance laser communication, in which the signal-encoded laser light with longer wavelength is necessary due to diffraction. The coherent laser beams transparent within 5–15 μm region are preferable. Consequently, it is demanded to develop the high-efficient, easy-used, and low-cost mid-to-far IR laser devices, in which the IR NLO materials play the key role. The special advantage of the crystalline solid IR NLO materials lies in the production of all-solid state IR laser devices, which are portable and stable in practical applications.

In 1971, Chemla demonstrated the second harmonic generation (SHG) effect of silver thiogallate ($AgGaS_2$) crystal in the IR region [2]. $AgGaS_2$ can be optically transparent from 0.47 μm to 13 μm, and it belongs to $\overline{4}2$ m point group and it is a negative uniaxial crystal. The second-order nonlinear coefficient measured by Boyd showed that d_{36} at 10.6 μm is 11.1 pm/V [3], which is about 30 times larger than the d_{36} coefficient at 1.064 μm of the typical UV-vis NLO crystal, potassium dihydrogen phosphate (KDP). Up to now, $AgGaS_2$ crystal is the most common and representative IR NLO crystal and has been widely used in many areas [4, 5]. $AgGaS_2$ crystal is a typical I–III–VI chalcopyrite semiconductor with an energy gap of 2.7 eV. The laser-induced surface damage threshold (I_{thr}) at 10.6 μm is 0.1–0.2×10^{-12} W/m^2 with 150 ns pulse [6]. As a comparison, the laser damage threshold of KDP crystal at 1.064 μm (stronger laser beam) is 3–6×10^{-12} W/m^2 with 20 ns pulse [5]. The lower laser damage threshold limits the IR applications of $AgGaS_2$ crystal because it is easier to be destroyed by the high-power laser beam (basically due to the instant multiple-photon absorptions and/or Raman resonance absorptions). And thus, the laser devices produced by it are less durable.

Zinc germanium phosphite ($ZnGeP_2$) is another ternary chalcopyrite semiconductor from II–IV–V group with the same point group and similar structure as $AgGaS_2$ crystal [7]. It has a much larger NLO coefficient of $d_{36} = 68.9$ pm/V at 10.6 μm [8], which is about seven times larger than that of $AgGaS_2$ crystal. It is transparent in the region of 0.65–13 μm, where it has sufficient birefringence for phase-matching. It has good mechanical property as well with Mohs hardness being 5.5. But its optical damage threshold is also very low with I_{thr} being 0.78×10^{-12} W/m² at 9.6 μm with 120 ns continuum laser pulse [9]. Furthermore, a stable growth of single crystal with high structural perfectibility and uniformity is very difficult [10], which seriously limits the IR applications in laser devices.

Therefore, the two important factors that restrict the applications of IR second-order NLO semiconductors are (a) the low optical damage threshold and (b) the difficulty in perfect single crystal growth. Although the studies of the UV-vis NLO crystals also encounter the two problems, the small energy gap and the necessary optical transparency in the IR region are specified to the IR NLO crystals.

The great efforts have been made in the last decades to overcome the above-mentioned limitations of the IR second-order NLO semiconductors. The element substitution is one of the methods of choice. Silver gallium selenide ($AgGaSe_2$) was demonstrated as the IR second-order NLO crystal by Chemla et al. [11]. It is another ternary semiconductor with chalcopyrite structure similar to $AgGaS_2$, but the sulfur element has been substituted by selenide. Comparing to $AgGaS_2$ crystal, it widens the optical transparency window up to 19 μm, enhances d_{36} (10.6 μm) coefficient to 33 pm/V, which is about three times larger than that of $AgGaS_2$ crystal. The substitution effect is obviously positive. However, the laser-induced surface damage threshold of $AgGaSe_2$ crystal is still small since the measured I_{thr} is $0.1–0.2 \times 10^{-12}$ W/m² at 10.6 μm with 150 ns continuum pulse [12]. Many examples can be found in the literatures.

In the recent years, besides the development of the novel growth techniques for perfect single crystal, the research focuses mostly on the enhancement of the laser damage threshold of the IR second-order NLO materials for practical applications. Although the relationship between the structure and optical damage threshold has not yet been clearly understood, some reports revealed that the enlarged energy gap (ΔE) could enhance I_{thr} because the larger ΔE would make the multiple photon absorption more difficult to be happened [13]. The larger ΔE could be obtained by introducing light elements into the compounds. One example is the substitution of the heavier transition-metal ions (like silver) by the alkali or alkaline metal ions in chalcopyrite semiconductors. Another choice is the substitution of sulfur or selenide by halogen group elements which possess the lone-pair electrons benefiting to the large second-order NLO effect. For instance, $NaSb_3F_{10}$ crystal reported by Qin and Chen [14] was discovered in terms of the above-mentioned two considerations. The I_{thr} of this crystal has been reported to be much larger than those of chalcopyrite semiconductors. The problem is that the IR transparent edge of this crystal has been reduced and the SHG effect has been decreased. The essential reason relates to the

transparency–nonlinearity trade-off relationship. The enlargement of ΔE would intrinsically reduce the d coefficient because they are inversely propositional to each other.

By the element substitution and structural modification, people have effectively tuned the SHG coefficients, transparency windows, and I_{thr} values. This structural tuning would be an important means in the further development of novel IR NLO materials in semiconductor family. Nevertheless, the transparency–nonlinearity trade-off incarnates in nonlinearity and optical damage threshold as well. In other words, the difficult choice between I_{thr} and d coefficient makes the space very limited of the discovery of the practical IR second-order NLO materials in semiconductors. It is obvious that new research area needs to be explored for developing the new-generation IR second-order NLO materials.

The IR optical materials are usually characterized by containing heavy elements. In the past decade, the second-order NLO materials containing transition-metal elements have attracted great interest. Di Bella in 2001 overviewed the transition-metal complexes (organometallic and coordination) as second-order NLO materials and pointed out that the transition-metal complexes offer a very large variety of structure and can satisfy different aspects of second-order NLO materials [15].

The studies on inorganic metal cluster compounds as the IR second-order NLO materials have been carried out in our research group for more than ten years, particularly by using the first principle computational studies on the structure–property relationship and material designing and simulations. The studies revealed that the polynuclear metal cluster compounds containing direct metal–metal bonding is a promising area in searching novel mid-to-far IR second-order NLO materials. Besides the various structures, high stability and diverse electronic property, the prior advantage of the metal cluster compounds is the metal-to-metal charge transfer contribution to the second-order NLO response. This advantage makes it possible to separate the optical absorption (usually caused by ligands in near-to-mid IR region) from the NLO response (could significantly caused by metal–metal interactions), which benefits to the solution of transparency–nonlinearity trade-off dilemma in semiconductor family. In this review article, we will present the recent advances in the first-principle computational studies on the second-order NLO properties of polynuclear cluster compounds and the elucidation of the structure–property relationship for the purpose of discovering new practical second-order IR NLO materials.

2   Metal Cluster Compounds for Second-Order Nonlinear Optics

The high value of molecular quadratic hyperpolarizability (β) is the prerequisite of a material to have the strong second-order NLO effect. The great efforts have been made on developing different NLO chromophores with high quadratic

hyperpolarizability [16–24]. By introducing the heavy transition metal into a pure organic donor–π–acceptor conjugated molecular architecture, the electron push–pull mechanism could be reinforced which benefits to the high molecular quadratic hyperpolarizability. Since the pioneering works of Frasier [25] and Green [26], the discovery has aroused the great interest in developing organometallic NLO chromophores for two decades (for a contribution before 1991, see, e.g., [27] and the references therein; for a contribution before 2001, see, e.g., [15] and the references therein) [28–34]. Some organometallic complexes have been found to have extremely large quadratic hyperpolarizabilities, good photochemical stability, comprehensive charge transfer ability, and tailoring flexibility of coordination ligand. The extensive studies have provided profound understanding of the mechanism for the second-order response of the organometallic [35–39] and inorganic mononuclear complexes [40–44]. The dominant second-order NLO mechanism of the organometallic chromophores lies in the intense, low-energy charge transfers between the metal centers and coordination ligands (MLCT/LMCT) [45–51]. In some particular condition, the metal-inductive ligand-to-ligand charge transfers (LLCT) or intraligand charge transfers (ILCT) can play the key role in second-order activities [52, 53] as well. These revealed that second-order NLO mechanisms all critically depend on the coordination ligands (L) which leads to the ineluctable exploitation on the extended conjugated ligands in developing organometallic NLO chromophores. For example, Le Bozec and his coworkers reported an octupolar zinc complex exhibiting very high quadratic hyperpolarizability ($\beta_{1.91} = 870 \times 10^{-30}$ esu and $\beta_0 = 657 \times 10^{-30}$ esu) [54]. The coordination ligand of this compound is the extended long ligand, 4,4$'$-oligophenylenevinylene-functionalized 2,2$'$-bipyridine which is responsible to the large β value originated from the MLCT process. Both experimental and theoretical studies came to the similar conclusion that the nature of coordination of conjugated ligands crucially influences the second-order response [23, 29–31, 55]. However, some reports further indicated the unfavorable red shifts of the low-lying charge transfer excitations into the visible part or even into the near-to-mid IR part of the spectra and the large dipole moments unfavorable to the noncentrosymmetric crystallization due basically to the extended π-conjugated coordination ligands. These drawbacks seriously restrict the practical nonresonant applications of large numbers of the organometallic NLO compounds in the IR region. The present challenge is to explore the metal-based NLO chromophores with an improved transparency–nonlinearity trade-off [56–58], which requires to simultaneously control the primary NLO property (the quadratic hyperpolarizability) and the secondary property (optical transparency) through the structural tuning. The potential new mechanism for the second-order response that is *independent* on the size and order of the coordination ligands is largely expected.

Some studies have implied the contribution to the optical nonlinearities of the *direct* metal–metal interaction of inorganic polynuclear metal clusters compounds [59–62]. In contrast to the organometallic chromophores, the charge transfer (CT) processes of polynuclear metal cluster compounds involved in the NLO response are notably diverse and complex. The metal–metal interaction CT process (MMCT) activated by the incident laser light related to the d_1–d_2 transitions makes significant

contributions to the second-order NLO activities, which will be discussed in detail
in the following sections. The understanding of this distinct contribution will cast a
new light on the rationalization of the role of the *direct* metal–metal interactions in
global NLO activity and will benefit to the exploration of the novel IR second-order
NLO materials [63]. This *ligand-independent* mechanism for the second-order
response can bring in an unprecedented way in tuning the quadratic hyperpolariz-
abilities of metal clusters in addition to the modifications of the ligating groups. It is
thus critically important to understand the mechanisms and the role that transition
metals play in the enhancement of the quadratic hyperpolarizability in the develop-
ment of the effective NLO-active chromophores which are essential in the design of
novel IR second-order NLO materials.

2.1 *Computational Method for Metal Cluster Compounds*

Many theoretical efforts have been made on the second-order NLO mechanism of
the organometallic complexes in the past two decades both at the semiempirical
level and in recent years within the first-principle theoretical frameworks [31, 35,
36, 46, 64–67].

The calculations of quadratic hyperpolarizability require the high-level compu-
tational techniques such as large basis sets and electronic correlation correction in
order to compare with the experimental results. In such cases, the fast-developed
density functional theory (DFT) becomes the method of choice for the transition-
metal-containing complexes owing to its ability to deal with the sizable molecules
and to take into account the complex many-body effects at an economic computa-
tional cost. However, some studies carried out by DFT studies reported the failures
in computing quadratic hyperpolarizabilities of the long molecules and extend
organometallic complexes because the DFT results tend to underestimate the
long-range electronic excitations [68–73]. For example, Bruschi et al. compared
ab initio and DFT calculations of the organometallic carbonyl complexes of M
$(CO)_5$ L (M = W, Cr, L = Py, PyCHO, Pyz, $PyzBF_3$, BPE, $BPEBF_3$), which
showed the serious overestimation of the DFT calculations on the quadratic
hyperpolarizability [74]. The chief point lies in the lack of the *exact* general
exchange–correlation (XC) functional to describe the various chemical phenomena.
The great efforts have been made to rectify the defect within the DFT framework in
order to obtain the reliable quadratic hyperpolarizability of the long molecules,
oligomers, and extended polymeric systems [75–79] The Becke's parameter-fitting
hybrid methods which take into account the HF "exact" exchange based on the
adiabatic connection method (ACM) is one of the pathways to improve the DFT
calculations of the quadratic hyperpolarizabilities. We described in the following
subsection a new computational approach based on hybrid DFT (*c*PW1PW91)
benchmark which is reliable to the quadratic hyperpolarizability of transition-
metal-containing systems.

2.1.1 One-Parameter Hybrid Functional: *c*PW1PW91

According to Kohn–Sham density functional theory, the molecular electronic energy could be divided into several terms:

$$E = E_T + E_V + E_J + E_{XC} \tag{1}$$

where E_T, E_V, and E_J are the kinetic energy, potential energy, and electron–electron repulsion energy terms, respectively. The nonclassical energy term E_{XC} accounts for the exchange energy arising from the antisymmetry of the wave function and the correlation of the individual electrons. E_{XC} could be divided into two parts namely the exchange and correlation parts:

$$E_{XC} = E_X + E_C \tag{2}$$

The hybrid E_{XC} functional with the fractional HF exchange and DF exchange along with DF correlation formulated by Becke has the general form as follows:

$$E_{XC}^{hybrid} = P_1 E_X^{HF} + P_2 E_X^{DFT} + P_3 E_C^{DFT} \tag{3}$$

To the case of Beck-style three-parameter functional (B3LYP) [80, 81] formula, 3 is written as follows:

$$\begin{aligned} E_{XC}^{B3LYP} = E_X^{LDA} + a_0\left(E_X^{HF} - E_X^{LDA}\right) + a_x \Delta E_X^{Beck88} + E_C^{VWN} \\ + a_c\left(E_C^{LYP} - E_C^{VWN}\right) \end{aligned} \tag{4}$$

where the parameter a_0 represents the ratio between the HF exchange and LDA local exchange, while a_x scales Beck88 gradient correction to LDA exchange. Similarly, the parameter a_c weights the LYP nonlocal correlation correction to the local VWN correlation functional. The three fractional parameters $\{a_0, a_x, a_c\}$ $(0 \leq \{a_0, a_x, a_c\} \leq 1)$ have been determined by fitting the G1 molecule set: $a_0 = 0.20$, $a_x = 0.72$, and $a_c = 0.81$. Unfortunately, B3LYP method gave bad results to the quadratic hyperpolarizabilities of long organic molecules reported in the literatures [70] and the metal complexes as well, due basically to the parameter optimization being performed in ground-state situation.

The new hybrid E_{XC} functional, on the basis of the assessments of various XC functional models, adopted the *m*PW model (Barone's modified Perdew–Wang 1991 exchange functional [82]) as the nonlocal exchange and the PW91 (Perdew–Wang gradient-corrected correlation functional [83]) for nonlocal correlation functional. Both the local exchange and correlation functionals used LDA model, Slater style for exchange, and VWN for correlation. Formula 4 comes to the following form:

$$E_{XC}^{hybrid} = E_X^{Slater} + a_0\left(E_X^{HF} - E_X^{Slater}\right) + a_X\Delta E_X^{mPW} + E_C^{VWN}$$
$$+ a_c\left(E_C^{PW91} - E_C^{VWN}\right) \tag{5}$$

Champagne et al. reported that for the long organic molecules, the correlation part in an XC functional has negligible effect on β, while the exchange part is mainly responsible [68]. Our results also showed that the a_0 is much more sensitive to β than the other two ones [73]. Consequently, it is reasonable to simplify the three-parameter fitting to the one-parameter fitting, i.e., $\{a_0, a_c\}$ are set to constant, $a_x = 1, a_c = 1 - a_0$. The minimum value of the mean absolute deviation (MAD, S) gives rise to the optimized a_0 parameter. Formula 5 came to the following:

$$E_{XC}^{hybrid} = E_X^{Slater} + a_0\left(E_X^{HF} - E_X^{Slater}\right) + (1 - a_0)\Delta E_X^{mPW} + E_C^{PW91} \tag{6}$$

The one-parameter a_0 has been determined by the optimization of the quadratic hyperpolarizability of a sample set consisting of 27 transition-metal-containing molecules. Due to the lack of the experimental results of the quadratic hyperpolarizability of the sample molecules, the CCSD/6-311+G(d)/SDD results were used as the gauge in the parameter a_0 fitting process.

Figure 1 showed the curve of MAD values (S) of the 27-molecule sample set with respect to a_0 parameter. The minimum S value was found at $a_0 = 0.40$. As the result, formula 6 became
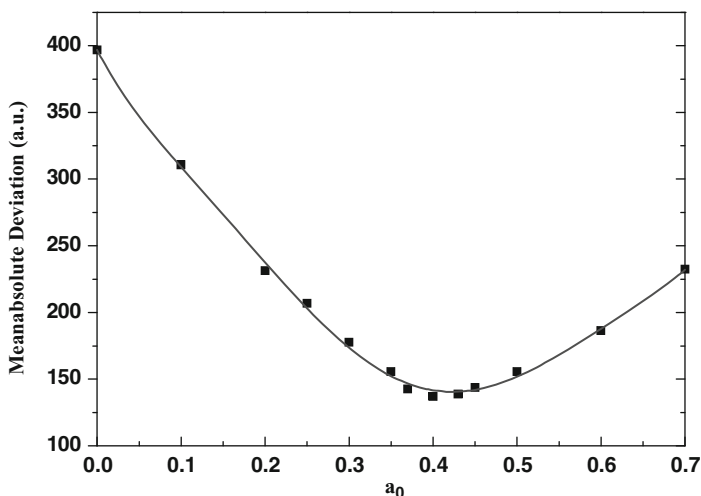

Fig. 1 Mean absolute deviation (MAD) of β values of the 27-moleucle sample set by fitting the parameter a_0. (This material is reproduced with permission of John Wiley & Sons, Inc. J Computational Chemistry 2009, 30, p.2061. ©[2009 Wiley Periodicals, Inc.])

Table 1 Calculated static quadratic hyperpolarizabilities (10^{-30} esu) of typical organometallic NLO chromophores using various computing models. (This material is reproduced with permission of John Wiley & Sons, Inc. J Computational Chemistry 2009, 30, p.2058. Copyright [2009 Wiley Periodicals, Inc.])

XC	W(CO)$_5$PyCHO	Cr(CO)$_3$Bz	FeCp$_2$COMe
SVWN	−5.52 (+47)	−25.43 (+179)	−0.96 (+38)
BLYP	−5.99 (+60)	−24.91 (+174)	−1.18 (+69)
BB95	−5.74 (+53)	−24.22 (+166)	−1.00 (+43)
BPW91	−5.67 (+51)	−24.04 (+164)	−0.95 (+36)
PW91PW91	−5.82 (+55)	−24.28 (+167)	−1.19 (+70)
mPWPW91	−5.75 (+53)	−24.16 (+165)	−1.04 (+49)
PBEPBE	−5.79 (+54)	−24.22 (+166)	−1.06 (+52)
mPW1PW91	−3.87 (+13)	−13.98 (+54)	−0.87 (+24)
B3PW91	−4.27 (+14)	−16.03 (+76)	−0.83 (+18)
B1LYP	−4.18 (+11)	−14.53 (+60)	−0.95 (+36)
B3LYP	−4.36 (+16)	−16.60 (+82)	−0.96 (+37)
M05	−4.11 (+10)	−14.74 (+62)	−1.00 (+43)
PBE1PBE	−4.28 (+14)	−14.08 (+55)	−0.84 (+20)
B97-2	−4.20 (+12)	−15.48 (+70)	−0.85 (+22)
BHandHLYP	−2.63 (−30)	−7.1 (−26)	−1.03 (+47)
HF	−1.28 (−66)	−2.19 (−75)	−0.32 (−54)
MP2	−3.13 (+17)	−6.43 (−29)	−1.72 (+146)
cPW1PW91	−3.92 (+5)	−9.28 (+2)	−0.80 (+14)
Expt.	−3.75	−9.10	−0.70

$$E_{XC}^{hybrid} = E_X^{Slater} + 0.40\left(E_X^{HF} - E_X^{Slater}\right) + 0.60\Delta E_X^{mPW} + E_C^{PW91} \quad (7)$$

Table 1 showed that this new one-parameter hybrid functional (named as cPW1PW91) could significantly improve the DFT performance in the computation of the quadratic hyperpolarizability of three typical organometallic complexes, W(CO)$_5$PyCHO, Cr(CO)$_3$Bz, and FeCp$_2$COMe. The improved accuracy indicates that the exact exchange functional is important in the description of excitation and NLO properties. This would illuminate the further development of the analytical XC functional in describing the electronic excitations and the NLO properties of the transition-metal-containing systems.

2.1.2 Orbital-Decomposition Analysis for Second-Order NLO Mechanism

The reliable theoretical calculations on the quadratic hyperpolarizabilities provide the important information in the analysis and understanding of the microscopic origin, NLO response mechanism, and structure–property relationship, which is critical to design and discover the novel second-order NLO materials.

The widely used two-level model comes from the "sum-over-state" method based on the perturbation theory, where the sum is simplified to only the ground

state and a single excited state. It takes into account a particular excitation in analyzing the contribution to static β of the electronic transition induced by the charge transfer.

$$\beta_{CT} \propto \frac{\Delta\mu_i M_i^2}{\Delta E_i^2} \tag{8}$$

where subscript i denotes the specified ith excited state. The $\Delta\mu_i$ is the difference of transition dipole moment between the ith excited state and the ground state. M_i is the transition dipole moment and ΔE_i is the transition energy from the ground state to the ith excited state. The two-level model still seems to be the useful and practical design rule for the NLO chromophores. However, the studies on the transition-metal-containing systems have been revealed that the two-level model is *invalid* any more to the extended and complex systems.

The orbital decomposition scheme firstly proposed by Hieringer and Baerends [84] is a very useful tool to relate the electronic structures and the relevant orbital-pair transitions to the quadratic hyperpolarizability. We have improved this decomposition to understand the second-order NLO nature of organometallic chromophores and coordination complexes. It can collect many important contributions which are missed by using the simple two-level model. The β value induced by the CT involving the relevant orbital-pair transitions was described as follows:

$$\beta_{(a,b)}^{CT} \propto \sum_i^N \frac{\Delta u_i c_{(a,b)} M_{(a,b)}^2}{\Delta E_i^2} \tag{9}$$

where (a, b) is an *occupied* to *virtual* orbital-pair transition involved in the ith excitation; $M_{(a,b)}$ is the corresponding transition dipole moment; $C_{(a,b)}$ is the weight factor of (a, b) transition. The summation is over N states that possess the (a, b) orbital pair. The $\Delta\mu_i$ could be obtained by using the finite-field method [66]. By using this scheme, the relative contribution to β_{CT} of a specified orbital-pair transition with respect to that of another one can be clearly shown.

Another advantage of the decomposition scheme lies in the economic computational burden. It could be obtained as a by-product of the quadratic hyperpolarizability calculations without any additional computations. So it is particularly useful to the complex sizable systems like the polynuclear NLO chromophores.

2.2 Second-Order NLO Properties of Dinuclear Rhenium Clusters

We present in this subsection the study of the metal–metal interaction effect on the quadratic hyperpolarizabilities of two dinuclear rhenium clusters, $Re_2(allyl)_4$ and $Re_2(\mu\text{-}S)_2O_2(CH_2CMe_3)_4$. The electronic structures, electronic excitation, and

quadratic hyperpolarizabilities have been computed and analyzed with the use of the high-level DFT/TDDFT methods. The geometries and the first intense excitations agree with the relevant reported measurements. An unprecedented second-order NLO response mechanism was found and discussed in these dirhenium compounds featuring the contribution of the direct metal–metal interaction transition process. This contribution positively enhances the quadratic hyperpolarizability and relates to the intensity of the metal–metal interactions of the complexes.

2.2.1 Structures and Computational Details

The initial geometric structures of the two dirhenium models taken from the X-ray diffraction data [85, 86] (Fig. 2) were fully optimized with C_2 symmetric restriction to the local energy minima which have been confirmed by no imaginary harmonic vibration frequency. The twofold axes of both models were arranged to be along Cartesian z axes which are also identical to their dipole moment directions.

The geometric optimizations and ground-state self-consistent-field (SCF) calculations were proceeded at the triple-ζ split-valence Slater orbital-type basis set with two augmented polarization functions (TZ2P) and the "small" frozen core level: (Re:$4d$; O:$2s$; S: $2s$; N:$2s$). The Becke–Perdew (BP) pure general gradient approximation (GGA) XC functional [87, 88] was used with the local density approximation (LDA) part being VWN type [89, 90] including the Stoll correction [91]. The scaled-ZORA Hamiltonian [92–94] was used to take account of the relativistic effect in the calculations. All the calculations were performed with the Amsterdam density functional program (ADF) [95, 96].

The orientationally averaged static values of the polarizability (α) and quadratic hyperpolarizability (β) are defined as follows:

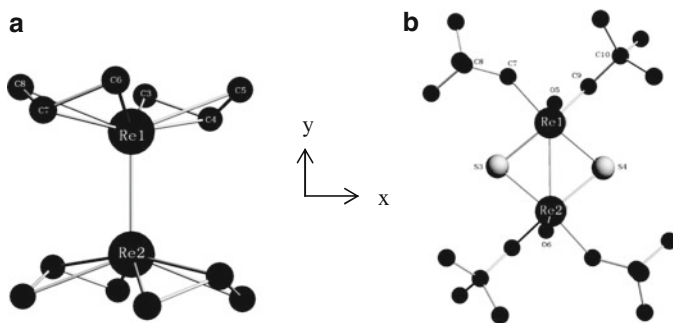$$\bar{\alpha} = \frac{1}{3}\left(\alpha_{xx} + \alpha_{yy} + \alpha_{zz}\right) \tag{10}$$

Fig. 2 Molecular structures of the models **1** and **2** (**a**) Re$_2$(allyl)$_4$; (**b**) Re$_2$(μ-S)$_2$O$_2$(CH$_2$CMe$_3$)$_4$. H atoms are omitted for clarity

$$\overline{\beta} = \sqrt{\sum_i \beta_i^2} \qquad (11)$$

$$\beta_i = \frac{3}{5} \sum_{j=x,y,z} \beta_{ijj}, \quad i = x, y, z \qquad (12)$$

Since the lack of the measured data available for the β of the two dirhenium complexes, the present computed values were largely qualitatively valuable. Based on this consideration, the solvent effects and intermolecular interactions, as well as frequency-dependent effects, which have been proved to be quantitatively important, are not included in the present qualitative evaluations of the quadratic hyperpolarizability.

2.2.2 Results and Discussions

Electronic Structures and Re–Re Bonding

The mean Re–Re bond distance in $Re_2(allyl)_4$ molecule (**1**) is 2.225 Å which was considered effectively triple by Cotton et al. [85]. The Re centers in the $Re_2(\mu\text{-}S)_2O_2(CH_2CMe_3)_4$ molecule (**2**) have square-pyramidal geometries with the oxo ligand in the apical position and the basal plane defined by two carbons and bridging sulfide group. The Re–Re distance of 2.759 Å is slightly longer than the sum of two Re atomic radii (2.741 Å), which was considered as single bond by Hoffman et al. [86]. The optimized geometric parameters are in reasonable agreement with the experimental data.

Mayer bond-order method (Table 2) [97] was adopted to analyze the bond properties. The bond order of Re–Re of model **1** is 2.20. On the contrary, the calculated Re–Re bond order is 0.65 indicating the much weak interaction between two rhenium atoms in model **2**. The results show the strong Re–Re bonding in model **1** and the weak Re–Re interaction in model **2**, which agree with the experiments.

The frontier molecular orbitals of model **1** are mostly composed of the $5d$ orbitals of dirhenium. For example, the HOMO (abs. as H) mainly locates on two

Table 2 Selected bond orders of models **1** and **2** obtained by Mayer method

1		**2**	
Re1–Re2	2.00	Re1–Re2	0.65
Re1–C3	0.33	Re1–S3	1.01
Re1–C4	0.58	Re1–S4	0.93
Re1–C5	0.33	Re1–O5	1.79
Re1–C6	0.33	Re1–C7	0.74
Re1–C7	0.58	Re1–C9	0.77
Re1–C8	0.33		

Re atoms with typical δ metal–metal antibonding orbital character (noted as $d_{mm\delta*}$) in agreement with the semiempirical result of Cotton et al. The HOMO of model **2** on the other hand locates on both the dirhenium atoms and the sulfide ligands. The LUMO (abs. as L) of model **2** has $d_{mm\sigma*}$ character as well as $p\sigma^*$ antibonding of oxo ligand.

Electronic Excitations

The gas-phase excitation spectra of models **1** and **2** are depicted in Fig. 3. The intense lowest-energy excitation peak (λ_{max}) of model **1** locates at 461 nm ($f = 0.01$). It mainly consists of the orbital-pair transition (H, L + 2) (99%) from the HOMO to the LUMO + 2. As mentioned, the HOMO locates on the two equivalent Re atoms with the metal–metal antibonding orbital character $d_{mm\delta*}$ and the LUMO + 2 also mainly locates at the two Re atoms but with the metal–metal π antibonding orbital character (noted as $d_{mm\pi*}$). Consequently, the λ_{max} of model **1** at 461 nm involves the $d_{mm\delta*} \rightarrow d_{mm\pi*}$ transition. The λ_{max} of model **2** locates at 546 nm which red-shifts 85 nm to that of model **1**. It has a slightly weak intensity of the calculated $f = 0.008$ and mainly composes of the orbital-pair transition of (H, L + 1). The HOMO is characterized by the p orbitals of the S atoms and the carbon atoms of L fragments (noted as L_σ) and metal–metal δ bonding (noted as $d_{mm\delta}$) of dirhenium. The LUMO + 1 mostly consists of the 5d orbital components of two Re atoms with $d_{mm\sigma*}$ character and a small percent of $p\sigma$ antibonding orbital components of oxo ligand ($L_{\sigma*}$). Consequently, The CT processes involved in λ_{max} transition are from ($L_\sigma + d_{mm\delta}$) to ($d_{mm\sigma*} + L_{\sigma*}$).
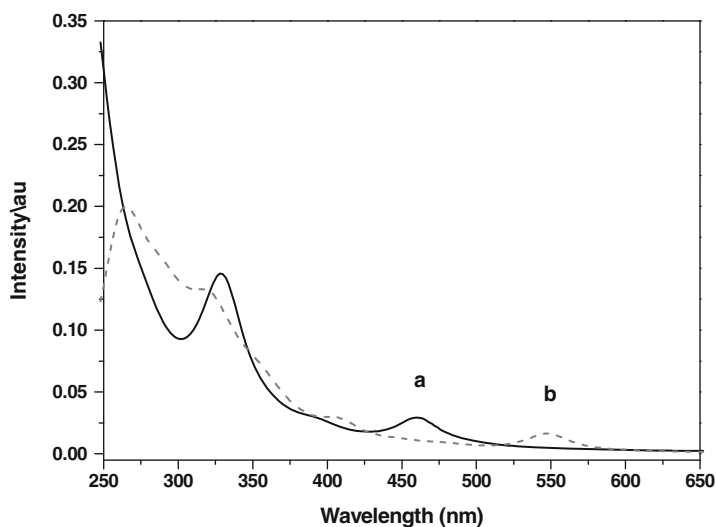

Fig. 3 Simulated electronic excitation spectra of (**a**) model **1** (*line*) and (**b**) model **2** (*gray dash*)

The measurements of the UV-vis spectra of these two cluster compounds at present are not available. Eglin and his collaborators have reported the intense lowest-energy absorption of another strong Re–Re coupled cluster $[Re_2Cl(NCN)_4]$ $[BF_4]$ (Re–Re distance is 2.224 Å which is very closed to that of model **1**, 2.225 Å) located at 460 nm with typical $d \rightarrow d$ transition character [98]. Some other available reports also give rise to the λ_{max} at around 420 nm–470 nm of some dirhenium complexes containing strong Re–Re interactions [99, 100].

Polarizabilities and Quadratic Hyperpolarizabilities

The calculated polarizability matrices of models **1** and **2** are almost diagonal, i.e., $\alpha_{ij} = 0$ $(i \neq j)$. The spatially averaged $\overline{\alpha}$ value of model **1** is 33×10^{-24} esu which is about one half of that of model **2** $(67 \times 10^{-24}$ esu).

The anisotropy of the calculated static β_i values of both models is obvious $(\beta_z \gg \beta_x, \beta_y)$ due to the specified molecular Cartesian coordinates. The quadratic hyperpolarizability of model **1** $[\beta_z(\mathbf{1}) \approx \overline{\beta}(\mathbf{1}) = 0.6 \times 10^{-31}$ esu$]$ is about one order of magnitude smaller than that of model **2** $[\beta_z(\mathbf{2}) \approx \overline{\beta}(\mathbf{2}) = 7.0 \times 10^{-31}$ esu$]$. The result is a surprise in that the second-order NLO response of model **1** with strong Re–Re interaction is much smaller than that of model **2** which contains weak Re–Re interaction.

The orbital decomposition analysis scheme has been executed to reveal the contributions of the particular occupied-virtual orbital-pair transitions (a, b) to a given quadratic hyperpolarizability as well as the corresponding CT processes involved in the transitions. The relevant orbital-pair transitions of polyatomic model **1** are multicomponent. The main contribution of the first four major orbital-pair transitions in magnitude order is that $(H - 1, L + 6)$, $(H - 4, L + 3)$, $(H - 2, L)$, and $(H - 1, L + 1)$ have the positive signs, while the fifth one $(H, L + 4)$ has the negative sign as illustrated in Fig. 4a. They are all obviously characterized by predominant metal-to-metal transitions relating to MMCT processes. The orbital pair $(H - 1, L + 6)$ has the largest positive contribution (the relative ratio is assumed as 100%). It is involved in the relative high-energy excitations (in the range from 4.9 to 6.1 eV). We note that it is *excluded* in the optically intense excitation (λ_{max}). The result conflicts with the assumption of the traditional two-level model which assumes that only the lower energy transitions are counted. The occupied $H - 1$ is the δ bond orbital of dirhenium $(d_{mm\delta})$ while the virtual $L + 6$ is dominant by π antibond orbital of dirhenium $(d_{mm\pi*})$ with the fractional components of $p\sigma^*$ orbitals of the allyl ligands $(L_{\sigma*})$ as shown in Fig. 4a. This orbital-pair transition therefore involves the MMCT $(d_{mm\delta} \rightarrow d_{mm\pi*})$ and MLCT $(d_{mm\delta} \rightarrow L_{\sigma*})$ processes. The former process is obviously predominant (~80%). The analyses showed that the following two orbital-pair transitions of $(H - 4, L + 3)$ and $(H - 2, L)$ have the second and third largest contribution to the $\overline{\beta}$ with the relative ratio of 88% and 51%, respectively. Both mainly involve MMCT with $d_{mm\pi} \rightarrow d_{mmsd*}$ and $d_{mm\pi} \rightarrow d_{mm\sigma*}$ characters, respectively $(d_{mmsd*}$ denotes
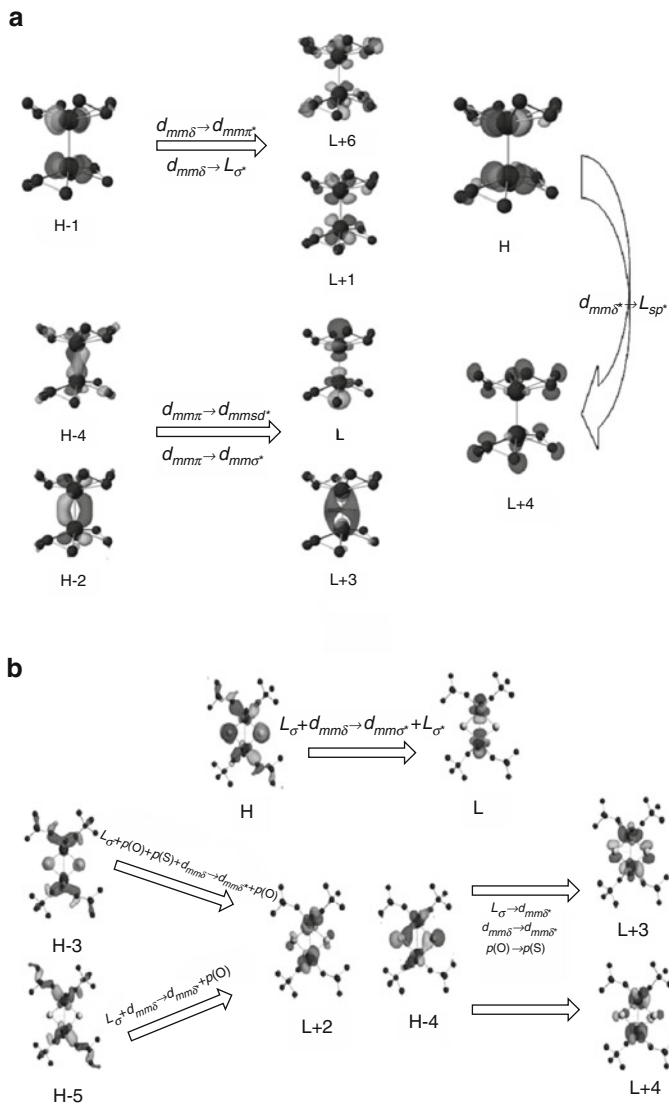
a

$d_{mm\delta} \to d_{mm\pi*}$
$d_{mm\delta} \to L_{\sigma*}$

H-1

L+6

L+1

H

$d_{mm\delta*} \to L_{sp*}$

H-4

$d_{mm\pi} \to d_{mmsd*}$
$d_{mm\pi} \to d_{mm\sigma*}$

L

H-2

L+3

L+4

b

$L_\sigma + d_{mm\delta} \to d_{mm\sigma*} + L_{\sigma*}$

H

L

H-3

$L_\sigma + p(O) + p(S) + d_{mm\delta} \to d_{mm\delta*} + p(O)$

$L_\sigma \to d_{mm\delta*}$
$d_{mm\delta} \to d_{mm\delta*}$
$p(O) \to p(S)$

L+3

H-5

$L_\sigma + d_{mm\delta} \to d_{mm\delta*} + p(O)$

L+2

H-4

L+4

Fig. 4 Illustrations of the orbital-pair transitions relevant to the quadratic hyperpolarizability of model **1** (**a**) and **2** (**b**)

the *sd* hybrid antibonding orbital of dirhenium [101]). Another orbital pair (H − 1, L + 1) with relative ratio (23%) is similar to (H − 1, L + 6). It involves predominated MMCT ($d_{mm\delta} \to d_{mm\pi*}$) and fractional MLCT ($d_{mm\delta} \to L_{\sigma*}$) characters. It is worth noting that there exhibits a negative contributor, the orbital pair (H, L + 4). It has a nonneglectable relative ratio of about −28% to the largest one. The HOMO locates on the dirhenium with typical δ antibond character as

mentioned above while the LUMO + 4 locates mostly on the allyl ligands. This orbital-pair transition therefore mainly involves MLCT ($d_{mm\delta*} \rightarrow L_{sp*}$), where L_{sp*} denotes the sp hybrid antibonding orbitals of allyl ligands. In a word, the metal-to-metal transition processes predominate over the $\bar{\beta}$ of model **1** while the MLCT process could be unfavorable to the enhancement of the quadratic hyperpolarizability.

The decomposition scheme performed on model **2** shows that there are three orbital-pair transitions contributing to β with positive signs while there are two with negative signs. The (H, L) transition has the largest contribution (100%). It is solely involved in the first dark excitation and is again excluded from the λ_{max}-related excitation. As depicted in Fig. 4b, the HOMO of model **2** is no longer dominated by the 5d orbitals of dirhenium, instead it has large components of the p orbitals of S atoms and CH$_2$CMe$_3$ ligand fragments: HOMO(**2**) $\approx 0.48p$(S) + 0.27p(L) + 0.12d (Re–Re). The LUMO in contrast to the HOMO is dominated by the $d_{mm\sigma*}$ orbitals of dirhenium with the nonnegligible fractional contribution from the ligands, which is mostly characterized by the atomic p antibonding orbitals of O atoms: LUMO (**2**) $\approx 0.78d$(Re–Re) + 0.20p(O). Consequently, the orbital-pair (H, L) transition has ($L_\sigma + d_{mm\delta}$) $\rightarrow$ ($d_{mm\sigma*} + L_{\sigma*}$) character. The relevant transition processes are multiple, i.e., the dominant LMCT ($L_\sigma \rightarrow d_{mm\sigma*}$) and the fractional MMCT ($d_{mm\delta} \rightarrow d_{mm\sigma*}$) and metal-inductive LLCT ($L_\sigma \rightarrow L_{\sigma*}$). The second largest contribution comes from orbital pair (H − 3, L + 2), where the HOMO − 3 involves [0.47p (L) + 0.23p(S) + 0.15d(Re–Re)] and the LUMO + 2 involves [0.55d(Re–Re) + 0.23p(O) + 0.18p(S)]. The orbital components of (CH$_2$CMe$_3$) ligands [p(L)] which are mainly involved in the occupied H − 3 (47%) is absent in the virtual orbital L + 2 indicating its electron donor character. The relevant electronic transition processes are again LMCT (dominant), MMCT, and LLCT. The third largest contribution comes from (H − 5, L + 2) transition. Different to H − 3 orbital, H − 5 mostly locates on CH$_2$CMe$_3$ ligand fragments and dirhenium without the component of p(O) and p(S). The relevant transition processes can be assigned to LMCT, MMCT, and LLCT as well. The CH$_2$CMe$_3$ ligand fragments clearly play the role as the electronic donor in the LMCT and LLCT and S and O atoms clearly play as the electronic acceptor in LLCT. The above three orbital-pair transitions make the positive contributions to the magnitude of β values. They give priority to LMCT processes but MMCT and metal-inductive LLCT processes are impressive. They are all involved in the lower energy excitations (in the range from 2.1 to 3.6 eV). On the other hand, the contribution of the orbital-pair transition (H − 4, L + 3) is the second largest in magnitude with the relative ratio of 74%, but it is negative, i.e., it would reduce rather than enhances the quadratic hyperpolarizability. This orbital-pair transition is involved in the higher energy excitations (in the range from 3.6 to 3.8 eV). The orbital HOMO − 4 has large components of p(O) and p(S). The d orbital components of dirhenium are only about 10% in total. In the virtual orbital L + 3 on the other side, the d orbital components of dirhenium enhance to 55% in total while the p(O) components decrease greatly. The relevant electronic transition processes are thus assigned to LMCT ($L_\sigma \rightarrow d_{mm\sigma*}$), MMCT ($d_{mm\delta} \rightarrow d_{mm\delta*}$), and LLCT [$p$(O) $\rightarrow p$(S)]. It is worth noting that the

contributions of the CH_2CMe_3 ligand fragments are absent. The other negative contributor is orbital pair $(H - 4, L + 4)$. Its contribution in magnitude has a relative ratio of about 18% to the largest one. The analysis shows the similar situation to that of orbital pair $(H - 4, L + 3)$ and will not be described in detail for clarity. It also involves the LMCT, MMCT, and LLCT processes missing the contribution of CH_2CMe_3 ligand fragments. In a word, the main CT process contributing to the quadratic hyperpolarizability of model **2** is LMCT process which is completely different to the situation in model **1**. If the CH_2CMe_3 fragments participate in the LMCT process as the electron donors in addition to the oxo and sulfide ligands, the contribution would be positive or vice versa. The MMCT has been confirmed to be one of the transition processes that play roles in the enhancement of the β values.

2.3 Second-Order NLO Properties of Trinuclear Anionic Clusters

In this subsection, we present the first-principle DFT calculations on the electronic excitations and second-order NLO properties in *solution phase* of two typical inorganic trinuclear anionic clusters, $[MoCu_2S_4(SPh)_2]^{2-}$ and $[Mo_2CuS_4]^{1-}(edt)_2(PPh_3)$ (edt = 1,2-ethanedithiolato). The computed excitation energies are in good agreement with the outcome of the measurements. The predicted values of the molecular quadratic hyperpolarizabilities are of the comparable order of those of the typical organometallic chromophores. We demonstrate again the significant contributions to the second-order responses from the charge transfers between the metal centers (MMCT) in these two charged clusters. This meaningful *ligand-independent* mechanism for the second-order response largely relates to metal–metal bonding strength.

2.3.1 Structures and Computational Details

The two molybdenum–copper trinuclear anionic clusters have been chosen due firstly to the various structures in relation to the metal nd configuration and oxidation states in the copper–tetrathiomolybdate complexes. One is a linear-typed bivalent anionic cluster, $[(PhS)CuS_2MoS_2Cu(SPh)]^{2-}$ (**3**), and the other is a triangular univalent anionic cluster with the incomplete cubane-like cluster core, $[Mo_2CuS_4]^{-1}(S_2C_2H_4)(PPh_3)$ (**4**) [102, 103]. The second feature lies in the similar Mo–Cu bonding in these two charged clusters possessing the different metal-core configurations (linear-typed vs. triangular, see Fig. 5). The original structures came from the X-ray diffraction data. In view of the metal–metal interaction, both clusters exhibit weak *direct* metal–metal interactions. Cluster **3** contains a pair of equivalent Mo–Cu bonds slightly shorter than the sum of atomic radii. Cluster **4** contains two inequable Mo–Cu bonds and an additional Mo(1)–Mo(2) bond. Although the metal–metal distances in cluster **4** are slightly larger than the sum
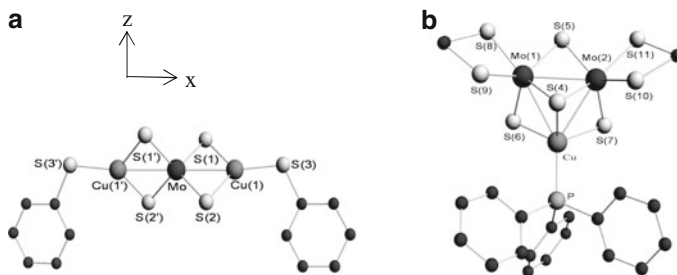
Fig. 5 Molecular structures of the anionic clusters (**a**) [(PhS)CuS₂MoS₂Cu(SPh)]²⁻, (**b**) [Mo₂CuS₄]¹⁻(S₂C₂H₄)(PPh₃). H atoms are omitted for clarity

of atomic radii, the *direct* weak metal–metal bonding interactions are generally considered [103].

The molecular geometries of clusters **3** and **4** were fully optimized in acetonitrile solution to the local energy minima which have been confirmed by no imaginary harmonic vibration frequency. The computed geometric parameters such as the bond lengths and angles are in reasonable agreement with the reported X-ray diffraction data. The optimizations and ground-state SCF calculations were proceeded at the TZ2P Slater-type orbital basis set with two augmented polarization functions and the "small" frozen core level: (Mo:3d; Cu: 2p; O:1s; S:2p; N:1s). The BP pure GGA XC functional was used with the LDA part being VWN type including the Stoll correction. The scaled-ZORA approximation of the relativistic theory was used. The solvent effects were employed in this study by using conductor-like screening model (COSMO) [104–106] of solvation with the Klamt surface [107]. The solute dielectric constant were set to 37.5 (MeCN, acetonitrile) for both models. The electronic excitation properties and the quadratic hyperpolarizabilities were calculated by using the response theory implemented in the RESPONSE module of ADF program. The GGA part of the XC functional employed the GRAC of the potentials based on the BP functional and the shape-corrected LB94 potential. Only the static β values of two models were calculated due to the absence of the comparative experimental dynamic data. Based on this consideration, the frequency-dependent effects as well as intermolecular interaction effects which have been proved to be quantitatively important are not included in the present qualitative evaluations of the quadratic hyperpolarizabilities.

2.3.2   Results and Discussion

Electronic Structures and Metal–Metal Bonding

The optimizations in solution can ensure the valid equilibrium structures for the solution-phase calculations of the electronic excitations. The small difference from the crystal structures can be explained by the presence of the intercluster

interactions in solid state. Cluster **3** has C_2 point group symmetry with z axis being the twofold axis. The central molybdenum atom is fourfold coordinated by four bridged sulfur atoms [μ_2-S(1, 2)]. Each copper atom is threefold coordinated by two μ_2-S(1, 2) and one terminal sulfur atom [t-S(3)]. The fragmental core MoS(1)S(2)Cu(1) is almost planar. And the structure features that the two equivalent planar cores [MoS(1)S(2)Cu(1) and MoS(1′)S(2′)Cu(1′)] are perpendicular to each other. The π-conjugated phenyl ring (noted as Ph in the following) connects to copper via t-S(3) with an angle of $\angle$Cu-S(3)-Ph $= 111.0°$. The distance between Mo and Cu atoms (2.669 Å) is about 0.03 Å longer than the sum of atomic radii ($r_{\text{Mo–Cu}} = 2.639$ Å). Cluster **4** features a near-regular trigonal fragmental core Mo(1)Mo(2)Cu. Each Mo atom coordinates to five sulfur atoms in a tetragonal-pyramidal manner. The Mo atoms directly connected to two edt ligands [$S_2(CH_2)_2$]. The sole Cu atom is tetrahedrally coordinated by three sulfur atoms and one PPh$_3$ ligand. Cluster **4** has two inequivalent Mo–Cu bondings in contrast to cluster **3** does, and it has an additional Mo(1)–Mo(2) bond. Mo(1)–Cu and Mo(2)–Cu distances (2.792 Å and 2.807 Å, respectively) are about 0.16 Å longer than the sum of atomic radii, and Mo(1)–Mo(2) distance is 0.15 Å longer than the sum of atomic radii ($r_{\text{Mo–Mo}} = 2.726$ Å).

The frontier molecular orbitals of polyatomic clusters **3** and **4** are multicomponent. The description will be emphasized for clarity on the metal characters and the metal–metal bonding properties. The *occupied* molecular orbitals of cluster **3** are characterized by the 3d valent orbitals of Cu atoms (noted as d_{Cu}) and 3p orbital of the sulfur atoms (noted as p_S). The Mo character is absent in the first three occupied MOs. The p–π orbitals of phenyl rings of PPh$_3$ ligands (noted as π_{Ph}) are present but minor. On the contrary, the 4d valent orbitals of Mo atoms (d_{Mo}) are dominant in the first three *unoccupied* molecular orbitals. The orbital component of MoS$_4$ fragment in LUMO is about 80%, while d_{Cu} are also present but is minor while p_S [t-S(3)] and π_{Ph} are absent. The anti-π bonding (noted as $d_{\text{mm}\pi*}$) and anti-δ bonding (noted as $d_{\text{mm}\sigma*}$) can be clearly found indicating the *direct* Mo–Cu interactions. The first two occupied MOs of cluster **4** are characterized by p–π orbitals of the *edt* ligands (p_{edt}) with a small amount of d_{Cu}. The third one (HOMO − 2) on the other side is characterized by the weak Mo(1)–Mo(2) π-bonding orbital (noted as $d_{\text{mm}\pi}$) with a small component of d_{Cu}. The first three *unoccupied* MOs are dominant by the Mo(1)–Mo(2) antibonding. Mo(1)–Mo(2) anti-δ bonding (noted as $d_{\text{mm}\delta*}$) presents in LUMO, $d_{\text{mm}\pi*}$ presents in LUMO + 1, and $d_{\text{mm}\sigma*}$ presents in LUMO + 2. Since there are single bonds between Mo and μ-S atoms (S$_4$–S$_7$), it is better to analyze the character of the Mo$_2$S$_4$ fragment as a whole rather than the separate Mo atoms and μ-S atoms.

Electronic Excitations

The computed vertical singlet excitation energies of models **3** and **4** in solution phase are illustrated in Fig. 6. The excitation bands of the trinuclear clusters are multicomponent. For concise, the emphasis is put on the main characteristics of each band as well as the calculated energies in comparison with the measurements.
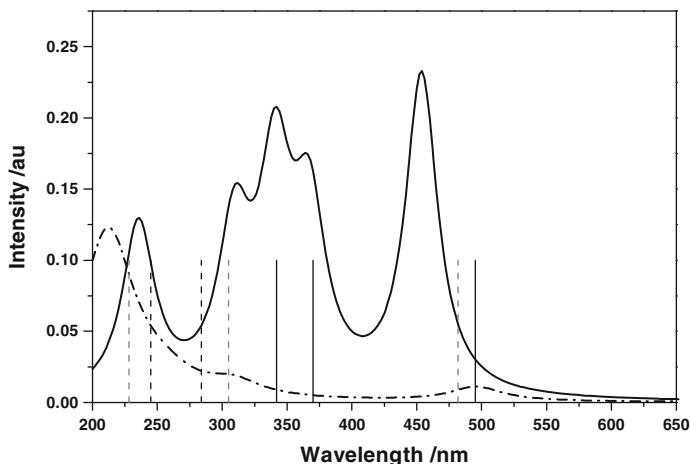
Fig. 6 Simulated electronic excitation spectra of anionic clusters **3** (line) and **4** (*dash dot*) in solution phase. The experimental excitation energies (*vertical line* for cluster **3** and *vertical dot* for cluster **4**) are also illustrated

Cluster **3** was computed to have five distinct absorption bands centering at 456 nm (v_1), 361 nm (v_2), 331 nm (v_3), 312 nm (v_4), and 235 nm (v_5). The calculated results agreed well with the measured data obtained in acetonitrile solution, i.e., 495 nm, 370 nm (sh), 342 nm, 284 nm, and 245 nm, respectively [102]. The analyses provide detailed orbital-pair transitions involved in the excitaion bands. The lowest-energy band v_1 (λ_{max}) contains three vertical excitations in a narrow energy range (2.68 eV–2.82 eV). It mainly originates from the charge transfers from t-S(3) and Ph ligand to the central Mo atom charactering the LMCT. v_2 band contains two intense excitations with the energies of 3.42 eV and 3.43 eV. The MLCT character is dominant with the CT from [MoCuS] cores to Ph rings. v_3 band contains three excitations with the energies from 3.68 to 3.86 eV. The main CT involved is MLCT ([MoCuS] fragment → Ph rings) while LLCT characters the minor CT process [t-S(3) → μ-S(1,2)]. v_4 band contains only one excitation (3.97 eV) which agrees well with the measured data of 284 nm. It manily involves the typical MLCT ([MoCuS] → Ph). The high-energy band v_5 contains two excitations with the energies of 5.24 eV and 5.36 eV. In addition to the typical MLCT involved in this band [CuS(1,2) → SPh], the d_{Cu}–d_{Mo} transitions are clearly presented. The MMCT (Cu → Mo) appears in the high-energy excitations.

The computed electronic excitations of cluster **4** display four intense bands. They are centered at 496 nm (v_1), 309 nm (v_2), 255 nm (v_3), and 212 nm (v_4), respectively. The three measured absorption bands are located at 482 nm, 305 nm, and 228 nm [103]. The theoretical values reasonably agreed with the experimental record except v_3 which was not observed in the measurement. The lowest-energy band v_1 (λ_{max}) contains single intense excitation, which is dominant by the d–p transitions with a small component of d_{Cu}–d_{Mo} transition. The CT processes involved in the excitation are short-distance MLCT/LMCT and weak MMCT

(Cu → Mo). v_2 band contains three vertical excitations in a narrow energy range around 4.02 eV. It characters the CT processes along the z axis from Mo_2S_4Cu core to Ph rings (MLCT) and *edt* to Ph rings (LLCT). v_3 contains six excitations, which are commonly characterized by the *p–p* transitions (*edt* → Ph and Ph → *edt*) and *d–p* transition (Mo_2S_4Cu → Ph). The high-enery band v_4 is realtively broad and intense containing nine singlet excitations in the energy range from 5.55 eV to 5.94 eV. It is dominant by the CT between metals (Cu → Mo) and the intra-*edt*-ligand CT [*edt* (S) → *edt*(C)]. The MMCT again appears in the high-energy excitations.

Polarizability and Quadratic Hyperpolarizabilities

The distinct structural anisotropy of two models has been sufficiently considered in assigning the Cartesian coordinates for the hyperpolarizability computations. The twofold axis of model **3** was arranged to be along z axis which is also identical to the dipole moment direction. The z axis of model **4** is along the direction of the vertical line of Mo(1)–Mo(2) bonding via Cu, and the xz plane contains the trigonal Mo(1) Mo(2)Cu core. As a result, the coordinate-dependent tensor components of polarizability and hyperpolarizability of both models exhibit the anisotropic characteristics. The polarizability tensor is almost diagonal ($\alpha_{ij} \approx 0$, $i \neq j$). The spatially averaged $\overline{\alpha}$ value of model **3** is 65×10^{-24} esu which is about two third of that of model **4** (92×10^{-24} esu). The static β_i values of the two models is remarkably anisotropic ($\beta_z \gg \beta_x$, β_y) resulting in $\beta_z \approx \overline{\beta}$. The quadratic hyperpolarizability of model **3** [$\beta_z(\mathbf{3}) \approx \overline{\beta}(\mathbf{3}) = 6.7 \times 10^{-30}$ esu] is about one half of that of model **4** [$\beta_z(\mathbf{4}) \approx \overline{\beta}(\mathbf{4}) = 16.0 \times 10^{-30}$ esu]. Since the absence of the experiental data of the quadratic hyperpolarizability, the computed quantities are only comparatively meaningful, i.e., model **4** possesses larger quadratic hyperpolarizability than model **3** does. And these values are modest and comparable to those of the typical organometallic NLO chromophores [15] such as that of metal carbonyl containing prindine or styrylpyridine ligands.

The contributions of the particular orbital-pair transitions (a, b) to β are unveiled by using the orbital decomposition scheme. The relevant orbital-pair transitions of model **3** are multicomponent. Figure 7 showed the dominant transitions and the their relative contributions. The (H, L + 8) transition makes the largest contribution to β_{zzz} (100%). It is mainly involved in the high-energy excitations (in the range from 4.9 eV to 6.1 eV). It is worth to note that this orbital-pair transition is again excluded from the lowest energy intense excitation (i.e., λ_{max}). The *virtual* LUMO + 8 is dominant by π^* orbitals of Ph rings ligands (ph$_{\pi*}$). This transition therefore involves the MLCT process [CuS(3) → Ph]. The second contribution came from (H − 2, L + 7) (53%), which also involves the MLCT similar to the first one. The typical $d_{Cu} \rightarrow d_{Mo}$ transition is the main character of the third contribution (21%) of (H − 9, L) transition. The MMCT (Cu → Mo) contribution to β value from this transition is impressive. The following contribution of (H − 3, L + 1) transition (14%) again exhibits the impressive MMCT character (Cu → Mo) which reinforces the MMCT contribution to the global β_{CT}. The (H − 2, L + 1) transition
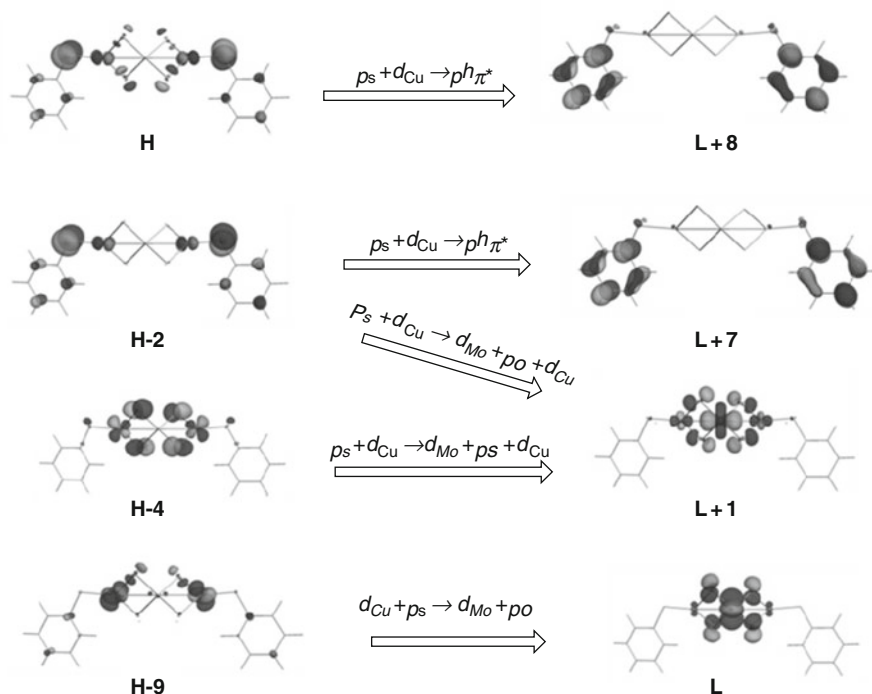
Fig. 7 Illustrations of the orbital-pair transitions and corresponding CT routes involved in the significant contribution to the quadratic hyperpolarizability of cluster **3**

has negative contribution (-19%) which is unfavorable to the global second-order response. The transition is a typical p–d transition involving the CT from SPh ligand to the MoS_4Cu core (LMCT). In summary, the multiple CT procesess are responsible to the origin of the second-order response of model **3** in which the MMCT process is confirmed with the positive contribution to global β value while the LMCT from the ligands to the metal core reduces the global β value.

There are six orbital-pair transitions mainly involved in the contribution of β value of cluster **4** (Fig. 8). The first two transitions, (H, L + 1) and (H − 1, L), have the larger contribution (100% and 68%, respectively) than the other four ones. (H, L + 1) transition characters the $p_{edt} \rightarrow d_{mm\pi*}$ transition involving the LMCT process ($edt \rightarrow Mo_2S_4$). The second (H − 1, L) contribution dominates the LMCT ($edt \rightarrow Mo_2S_4$) process similar to the first one. The following four orbital-pair transitions, i.e., (H − 6, L + 1), (H − 2, L + 5), (H − 5, L + 2), and (H − 5, L), have the similar mechanism, and one of them (H − 6, L + 1) is thus taken as the example. The HOMO − 6 possesses the significant metal charater of d_{Cu} and the p_{edt} [$0.22d(Cu) + 0.37p_{edt} + 0.11p(S) + 0.05p(P)$] while the *unoccupied* LUMO + 1 consists of a large component of $d_{Mo–Mo}$ with $d_{mm\pi*}$ character [$0.40d_{mm\pi*} + 0.06d(Cu) + 0.08p_{edt} + 0.27p(S)$] with the greatly reduced d_{Cu} and p_{edt} components. This transition involves the LMCT ($edt \rightarrow Mo_2S_4$) and MMCT
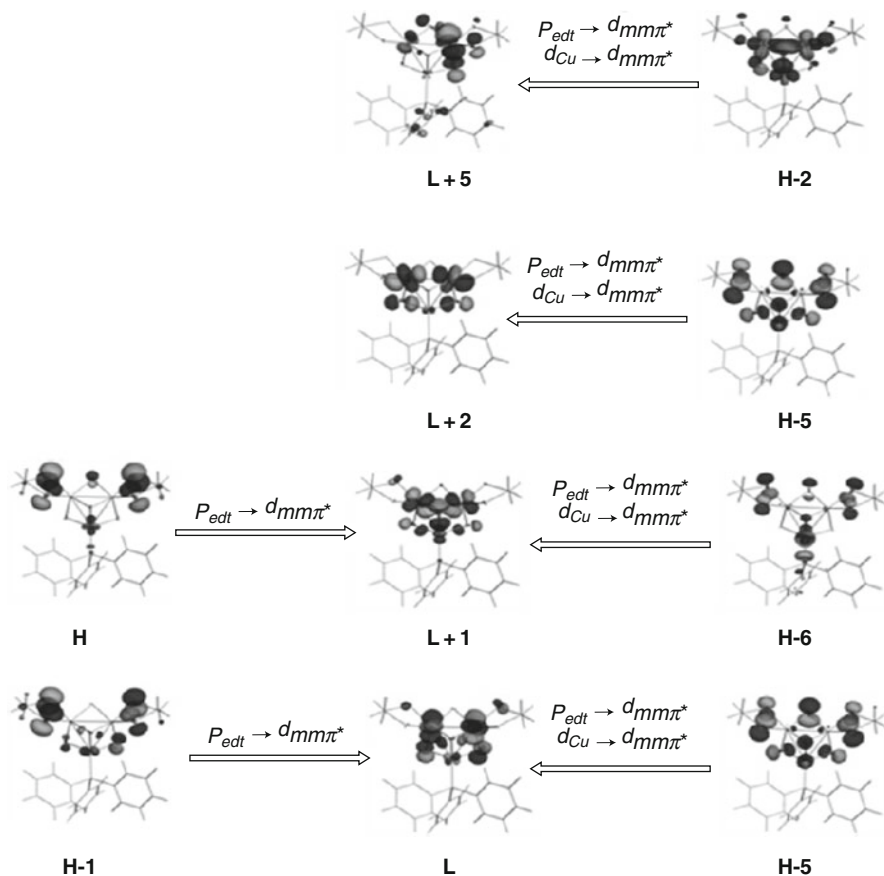
Fig. 8 Illustrations of the orbital-pair transitions and corresponding CT routes involved in the significant contribution to the quadratic hyperpolarizability of cluster **4**

$(d_{Cu} \rightarrow d_{mm\pi*}$, Cu $\rightarrow$ $Mo_2S_4)$, respectively. The later one is *nonnegligible* which once again exhibits the MMCT contribution to the second-order activity.

The MMCT processes in both models are significant for both models. The *ligand-independent* MMCT process is responsible to the fractional amount of global β_{CT} value particular in the case of model **4** of about 20%.

2.4 Second-Order NLO Properties of Pentanuclear Clusters

We present in this subsection the second-order nonlinear optical properties of a series of pentanuclear metal clusters $[MS_4Cu_4X_2Py_6]$ (M = Mo, W; X = Br, I) on the basis of the hyper-Rayleigh scattering (HRS) experiments and the first-principle

DFT calculations. The measurements obtain the notably large dynamic quadratic hyperpolarizabilities at 1,064 nm [$\beta(-2\omega, \omega, \omega)$ values are around 200×10^{-30} esu] and, by extrapolation, a large static values around 60×10^{-30} esu. The computational results of the electronic excitation energies and quadratic hyperpolarizabilities are in good agreement with the experimental. The in-depth analysis of the mechanism for the second-order response unambiguously shows the evidence of the contribution of *direct* metal–metal interaction charge transfers.

2.4.1 Experimental and Computational Details

HRS Measurement

The molecular quadratic hyperpolarizabilities of the four pentanuclear clusters, namely, [$MS_4Cu_4X_2Py_6$] (M = W, X = Br for **5** and I for **6**; M = Mo; X = Br for **7** and I for **8**) have been determined by HRS technique [108, 109]. The external reference method was utilized in the measurements by choosing *para*-nitroaniline (*p*NA) as standard. The measurements were carried out in dimethylformamide (DMF) solutions at 1,064 nm fundamental wavelength pumped from the optical parameter oscillation (OPO) by the Q-switched Nd:YAG laser (10 Hz, 8 ns pulse width). The laser radiation was focused by a cylindric lens (focal length 10 cm) into a quartz cell containing the samples. The HRS signals were detected by a fluorescence spectrometer containing a monochromator and a photo counter with high-degree of accuracy. The weak contributions of two-photon-induced fluorescence in the measurements were directly subtracted from total signal intensity to obtain the pure HRS signal by using a high-resolution monochromator near 532 nm. The solutions were sufficiently diluted (the condensations were below 4×10^{-4}) to ensure that absorption of scattered second-harmonic light was negligible.

The HRS results of the quadratic hyperpolarizabilities are frequency dependent. The corresponding inherent static values are extrapolated by using the two-level formulation [110]

$$\beta_{\mathrm{HRS}}^{0} = \beta_{\mathrm{HRS}}^{\lambda} \left[1 - \left(\frac{2\lambda_{\mathrm{max}}}{\lambda} \right)^2 \right] \left[1 - \left(\frac{\lambda_{\mathrm{max}}}{\lambda} \right)^2 \right] \tag{13}$$

where λ_{max} are the absorption maximum wavelengths of compounds and λ is laser radiation wavelength.

Structure and Computational Methods

The molecular geometries were fully optimized in DMF solution modeled by COSMO approach using the Klamt surface. The solute dielectric constant was 36.0 for DMF. The TZP Slater-type basis set was used with the frozen core scheme

of (W:4f; Cu:3p; S: 2p; N:1s). The BP XC functional was used with LDA part being VWN type including Stoll correction. The scaled-ZORA Hamiltonian was used to take account of the relativistic effect. The electronic excitations and the quadratic hyperpolarizabilities have been calculated in DMF solution by using GRAC potentials based on the shape-corrected LB94 potential. The Davidson diagonalization method has been used to yield the excitation information.

The HRS comparable values β_{HRS} are also calculated by using the formula deduced by Cyvin et al. [111] assuming Kleinman's symmetry and plane-polarized incident light:

$$\beta_{HRS} = \sqrt{\langle \beta_{ZZZ}^2 \rangle + \langle \beta_{XZZ}^2 \rangle} \tag{14}$$

where

$$\langle \beta_{ZZZ}^2 \rangle = \frac{1}{7} \sum_i \beta_{iii}^2 + \frac{6}{35} \sum_{i \neq j} \beta_{iii} \beta_{ijj} + \frac{9}{35} \sum_{i \neq j} \beta_{iij}^2 + \frac{6}{35} \sum_{ijk, \text{ cyclic}} \beta_{iij} \beta_{jkk} + \frac{12}{35} \beta_{ijk}^2$$

$$\langle \beta_{XZZ}^2 \rangle = \frac{1}{35} \sum_i \beta_{iii}^2 - \frac{2}{105} \sum_{i \neq j} \beta_{iii} \beta_{ijj} + \frac{11}{105} \sum_{i \neq j} \beta_{iij}^2 - \frac{2}{105} \sum_{ijk, \text{ cyclic}} \beta_{iij} \beta_{jkk} + \frac{8}{35} \beta_{ijk}^2$$

The full expression for β_{HRS} can be found in the reference [112].

2.4.2 Results and Discussion

HRS Results

The HRS results of the quadratic hyperpolarizabilities are summarized in Table 3. The two bromide clusters **5** and **7** have slightly different quadratic hyperpolarizabilities (β_{HRS}). Cluster **7** which is centered by Mo atom has a larger β_{HRS} than cluster **5** does which has W as the central metal atom. The condition is similar to the two iodate clusters. The $\beta_{HRS}(\mathbf{8})$ containing Mo central atom is about 20% larger than $\beta_{HRS}(\mathbf{6})$. On the other hand, clusters **6** and **8** coordinated to iodine atoms have much larger β_{HRS} values than clusters **5** and **7** does which are coordinated to

Clusters	β_{HRS}
[WS$_4$Cu$_4$Br$_2$Py$_6$] (**5**)	164
[WS$_4$Cu$_4$I$_2$Py$_6$] (**6**)	319
[MoS$_4$Cu$_4$Br$_2$Py$_6$] (**7**)	198
[MoS$_4$Cu$_4$I$_2$Py$_6$] (**8**)	354

Table 3 HRS experimental results of molecular quadratic hyperpolarizability (10^{-30} esu) in DMF solution of clusters **5**–**8** at 1,064 nm laser radiation

bromine atoms. For example, the $\beta_{HRS}(\mathbf{6})$ value is about twice as $\beta_{HRS}(\mathbf{5})$. This is understandable because of the larger ionic radius of iodine atom, although both iodine and bromine have the same number of valent p electrons. The lone-pair electrons in iodine ionic ligands could be more delocalized in the clusters which benefit to the electron donating. Conclusively, cluster **8** which contains both the iodine ligands and central Mo metal atom has the largest value of β_{HRS} among the four analogs, which agrees with HRS measurements. The $\beta_{HRS}(\mathbf{8})$ value of 354×10^{-30} esu is sizable, and it is about one-order magnitude larger than the typical tungsten carbonyl organometallic chromopores such as $W(CO)_5$(pyridine) [113].

Electronic Structures and Metal–Metal Bonding

The optimized molecular structures of the **5–8** clusters (Fig. 9) were all in agreement with the reported experimental data in solid state [114–116]. The optimizations performed in DMF solution simulate the experimental environments of both the UV-vis spectra and HRS measurements. The distances between the central metal M (M = Mo, W) and coppers (Cu_1/Cu_2) relaxed in the range of 0.04 Å for M–Cu_1 and 0.06 Å for M–Cu_2, respectively, after the restricted optimization. The M–Cu lengths are closed to those in [MoOS_3Cu_3Cl(PPh_3)_3] [2.705 Å–2.740 Å] which is reported to have weak Mo–Cu interactions [[117]]. The bond angles of Cu–M–Cu and Cu–M–Cu tend to be 90° and 180°, respectively, resulting in the quasiregular quadrangles of the planar MCu_4 cores. The optimized distances of M–S are slightly lengthened as well in the range of 0.03 Å to 0.05 Å. The overall pictures of the DFT optimized structures of the clusters depict the more compact clusters in general with the slightly relaxed metal cores. Table 4 listed the selected Mayer bond orders of the four clusters. It is interesting to see that the bond order of Mo(W)–Cu are around 0.3 to 0.4 indicating the weak *direct* M–Cu interactions in the clusters while the single
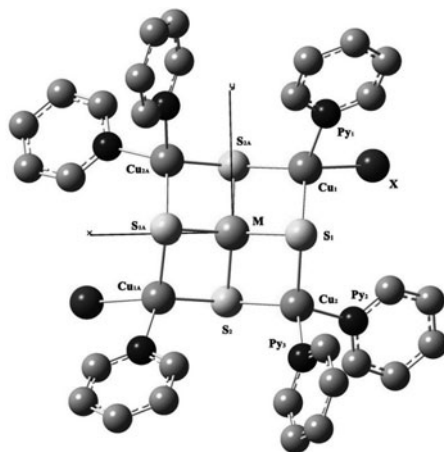

Fig. 9 Molecular structures and orientation of [MS_4Cu_4X_2Py_6] clusters, M = W, X = Br for cluster **5**; X = I for cluster **6**; M = Mo, X = Br for cluster **7**; and X = I for cluster **8**. H atoms are omitted for clarity

Table 4 Selected Mayer bond orders of clusters **5–7**

	5	**6**	**7**
M–Cu	0.4	0.4	0.4
M–S	1.1	1.1	1.1
Cu–S	0.6	0.6	0.7
Cu–Br/I	0.4	0.6	0.3
Cu–N(Py)	0.5	0.5	0.6

bonds between Mo(W) and S are clearly showed. The bond orders of Cu and their peripheral ligands (S, Br/I, and Py) are all around 0.5 in the range of coordination interactions.

The occupied frontier molecular orbitals of clusters **5–7** are all essentially localized on $Cu_1S_1XN(Py_1)$ and $Cu_2S_2N(Py_2)N(Py_3)$ fragments and their symmetric equivalents. The orbital overlaps between coppers and halogens are minor indicating the ionic interaction between them. The p-type orbitals of lone-pair electrons of the halogen are significant. The unoccupied MO exhibits the σ antibond orbitals of MS_4 core fragments. The LUMO of clusters **5** and **6** composes MS_4 σ^* orbitals, while for cluster **7**, both LUMO and LUMO + 1 contain this type of orbitals. The higher unoccupied MOs are essentially anti-π-conjugated MOs of the ancillary pyridine rings with only small components of MS_4 fragments. For clarity and simplicity, we analyze in detail the molecular orbitals of cluster **5**. The HOMO locates entirely on the $Cu_1S_1BrN(Py_1)$ and $Cu_2S_2N(Py_2)N(Py_3)$ and their symmetric equivalent units. The $3p_x$ orbitals of μ_3-S make σ bonds to $3d$ of Cu. The $4p_x$ of Br make *nonbond* to $3d$ of Cu_1. The HOMO is obviously irrelevant to the center metal W and Py rings. The LUMO resides mostly on WS_4 unit. The $3p$ (μ_3-S) make σ^* bonds to the $5d_{z2}(W)$ atom. The LUMO + 1 mainly locates on the WS_4 core as well. The $3p(\mu_3$-S) make π^* bonds to the $5d_{xy}(W)$. The situation for the other two clusters is similar.

Electronic Excitations

Table 5 listed the computed electronic excitations of clusters **5–7** in the range from 350 nm to 700 nm. The calculated excitation energies are in good agreement with the experimental outcome [114–116]. Cluster **5** has been measured to have two intensive absorptions at 442 nm and 334 nm, respectively. The calculated electronic excitation at 477 nm has 35 nm deviation for the former one, and the calculated 388 nm and 355 nm bands are close to each other with an averaged value of 371 nm which relates to the later one with a deviation of 36 nm. For clusters **6** and **7**, the deviations from the measured data are all within 40 nm.

The transitions composed in each intense excitation band are multiple and complex. Taking cluster **5** as an example, the lowest-energy exciation at 477 nm mainly involved three orbital-pair transitions of the (H − 7, L + 7), (H − 7,

Table 5 Most intensive excitations and oscillator strengths, f, of clusters **5**–**7** within the range between 350 nm and 750 nm

Cluster	Excitation	f	Expt.
5	477 nm	0.04	442 nm
	388 nm	0.03	334 nm
	355 nm	0.03	
6	478 nm	0.03	438 nm
	354 nm	0.09	316 nm
7	496 nm	0.03	526 nm
	355 nm	0.05	384 nm
	327 nm	0.03	298 nm

L + 5), and (H − 8, L + 4). The first transition is corresponding to the transition from 4p orbitals of two Br atoms to π orbitals of pyridine rings, which belongs to LLCT process. The second one is similar to the first one which belongs to LLCT as well. The third one is corresponding to the transition from the HOMO − 8, which is mainly localized on two Br atoms with small contributions of 4d orbitals of Cu_1/Cu_{1A} atoms to the LUMO + 4, which is mainly located on the Py rings. It belongs to LLCT (major) and MLCT (minor) process. Consequently, the lowest-energy absorption at 477 nm of cluster **5** is assigned to the LLCT (from p of LP to p–π of Py) and MLCT (from d of Cu_1 to p–π of Py) processes. Similarly, the lowest-energy excitations of clusters **6** and **7** have been assigned to LLCT (major) and MLCT (minor) processes as well. If the second-order response of these metal clusters was analyzed by the traditional two-level model which states that the β_{CT} is contributed by the intense lowest-enegy excitation, it could be ascribed to the LLCT (major) and MLCT (minor) processes missing the contribution of weak *direct* metal–metal interactions. However, the orbital-decomposition analysis gives rise to the quite different pictures of the mechanism for the second-order response of these metal clusters.

Polarizabilities and Quadratic Hyperpolarizabilities

The calculated dipole moments μ of clusters **5**–**7** are large and distinctively anisotropic. The dominant dipole components are along the z axis which is also the molecular twofold axis (crystalline c axis). The static polarizability matrices are almost diagonal. The average α values of clusters **5**–**7** are in the order of $\overline{\alpha}(\mathbf{2}) > \overline{\alpha}(\mathbf{3}) > \overline{\alpha}(\mathbf{1})$. Although all β tensor components have been calculated, Table 6 listed the representative quantities: the static spatial-averaged value $\overline{\beta}_0$ and β_{HRS} which could be comparable to the measured HRS data. The calculated β_{HRS} values are in good agreement with the extrapolated measured data. The order of the values in magnitude also reproduces the experiment: β_{HRS} (**6**) $> \beta_{HRS}$ (**7**) $> \beta_{HRS}$ (**5**).

The orbital-decomposition analysis on cluster **5** revealed that largest contribution (100%) to β was (H, L + 3) orbital-pair transition, which mainly came from the

Table 6 Dipole moments (debye), dipole static polarizabilities (10^{-24} esu), and static quadratic hyperpolarizabilities (10^{-30} esu) of clusters **5–7**

Cluster	μ	$\overline{\alpha}_0$	$\overline{\beta}_0 \sim \beta_z$	β_0 (HRS)	Expt.
5	18.2	101	25	40	42
6	18.8	108	41	62	75
7	18.3	103	33	46	58

excitations in the energy range from 1.95 eV to 2.00 eV. The second large contribution in magnitude came from the (H, L) transition (about 40% to the largest one). These two β_{CT}-related transitions have the lower excited energies and intensities than the intense absorption located at 477 nm (2.60 eV). However, these dark absorptions made major contributions to the quadratic hyperpolarizability. The LUMO + 3 is located on the Py_2 rings with small percentage on the WS_4 core, and HOMO and LUMO have been discussed. The CT processes related to the two orbital-pair transitions were thus assigned to the processes from the collective d–p system and the lone-pair p electrons to the planar coordination p–π ring ligands and d–p WS_4 core. The multiple CT processes are involved, and the synergic effects are obvious. The percent components of the HOMO, LUMO, and LUMO + 3 are approximated as 55%Cu(3d) + 20%S(3p) + 15%Br(4p) + 3%N (2p), 70%Py(π) + 10%W(5d) + 10%S(3p), and 50%W(5d) + 40%S(3p), respectively. These two transitions involved the MLCT [Cu(3d) $\rightarrow$ Py(π)], MMCT [Cu (3d) $\rightarrow$ W(5d)], and LLCT [Br(4p) $\rightarrow$ Py(π)] (see Fig. 10). The contribution of the weak W–Cu interaction to β-related CT is impressive in which the coppers play as electron donors and central tungsten as an acceptor. The later (H, L) transition, which is MMCT dominant, makes a positive global contribution of about 30% to the β_z value.

Cluster **6** presents similar results as cluster **5** but are more complex (Fig. 11). The dominant orbital-pair transition was again (H, L + 3). The second large contribution in magnitude came also from the (H, L) transition (about 85% to the largest one). The third large contribution in magitude came from the (H − 5, L + 3) transition with a relative contribution of about 40% to the largest one. The CT processes related to the first two dominant transitions are similar to the case of cluster **5** (from the collective d–p system of [$Cu_4S_4N_6$] unit and the LP p of iodine atoms to the p–π of Py ligands and the d–p of WS_4 core with MLCT, MMCT, and LLCT characters). The contributions of W–Cu weak interaction to the relevant CT are again impressive. The third transition involved the occupied HOMO − 5, which composed mainly of the p lone-pair orbital of iodine atoms and d orbitals of two Cu_1 atoms, and the virtual LUMO + 3 located on two Py_2 rings, and thus, the CT character was mainly the LLCT and MLCT.

For cluster **7**, the orbital-pair transitions that make largest contribution were the (H, L + 1) transition and the (H − 3, L + 2) transition, which gave rise to the second large one (about 11% to the largest one). The LUMO + 1 is mainly located on MoS_4 metal core. The CT processes related to the dominant transition were from the d–p system of [$Cu_4S_4BrN_6$(Py)] fragment to the d–p of MoS_4 core with the
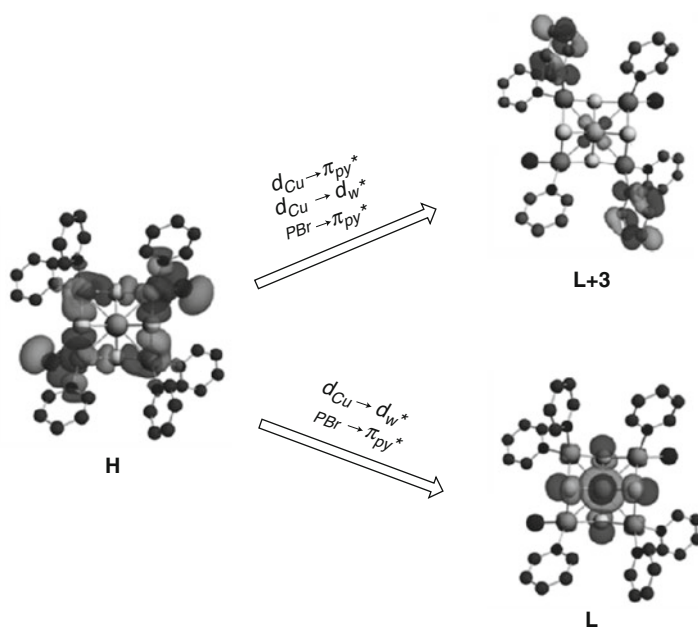
Fig. 10 Illustrations of the major orbital-pair transitions and corresponding CT routes involved in the significant contribution to the second-order responses of cluster **5**
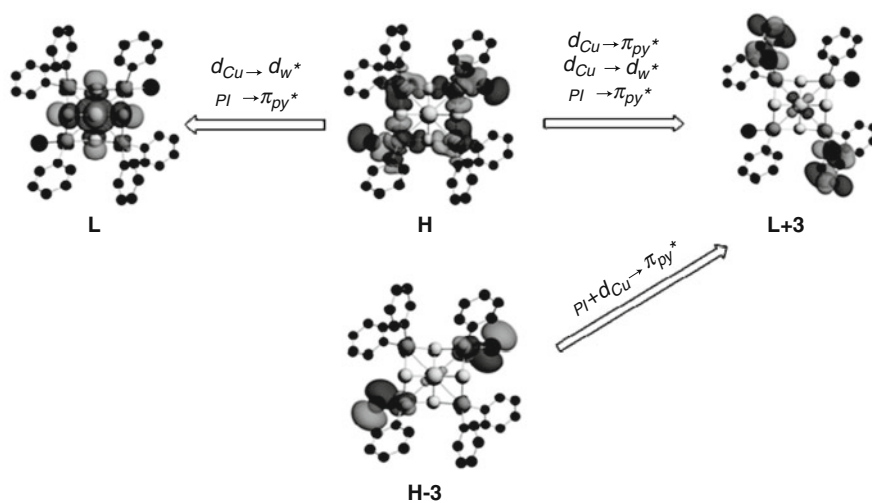

Fig. 11 Illustrations of the major orbital-pair transitions and corresponding CT routes involved in the significant contribution to the second-order responses of cluster **6**

significant character of MMCT and LLCT. The second transtion involved the charge tranfer from two $Cu_1S_1BrN(Py_1)$ fragments (HOMO − 3) to two Py_2 rings (LUMO + 2) shown in Fig. 12, and it was assigned to the typical MLCT [$Cu(3d) \rightarrow Py(\pi)$] and LLCT [$Br(4p) \rightarrow Py(\pi)$, $S(3p) \rightarrow Py(\pi)$] processes. Since the first transition is dominant, the contribution of Mo–Cu weak interaction CT is significant in cluster **7**.

In summary, the orbital-pair decomposition analysis gave rise to the multiple routes of the β-related CT processes and the cooperative effects contributed to the quadratic hyperpolarizabilities. The metal–ligand interactions and the metal-induced ligand–ligand interactions play the important roles in the global second-order activities similar to the cases of the organometallic chromophores. The halogen atoms with lone-pair p electrons played the roles as the electron donors in the relevant LLCT processes, while the π-conjugated pyridine ligands played the acceptors in the relevant MLCT and LLCT processes. However, the weak *direct* metal–metal interaction unambiguously involved in the β-determined CT process and in some cases even made the significant contribution (e.g., in cluster **7**), where the coppers act as the electron donors while the central metal atom (W/Mo) played the role of electron acceptor. The $3d(Cu) \rightarrow 5d(W)$ in the case of cluster **5** exhibiting the featured d_{Cu}–d_W transitions in the polynuclear metal clusters.

The large molecular β of these clusters are favorable to produce the large macroscopic NLO coefficients. The estimation of the second-order susceptibility $\chi^{(2)}_{zzz}$ of one of the cluster compounds (cluster **7**) in solid state in terms of the molecular quadratic hyperpolarizability has been performed on the basis of the oriented-gas approximation [118] with the fact that the z components of the dipole moment $\mu = \mu_z$ of the molecular clusters in a unit cell have an identical direction ($\theta = \phi = \varphi = 0$).
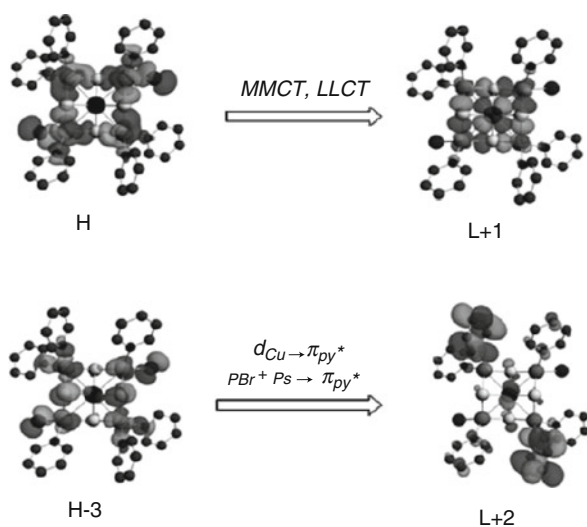

Fig. 12 Illustrations of the major orbital-pair transitions and corresponding CT routes involved in the significant contribution to the second-order responses of cluster **7**

$$\overline{\chi}_{zzz}^{(2)}(\omega) \approx NF^3 \beta_{zzz}(\omega) \cos\theta \cos\phi \cos\varphi \qquad (15)$$

where F is the local field factor and N is the molecular density ($N = 1 \times 10^{21}\,\mathrm{cm}^{-3}$ from the experimental data). F is assumed to 1 because the measured refraction indices of the crystals are not available at present. The HRS measured β value [$\beta_{\mathrm{HRS}}(\omega) = 319 \times 10^{-30}$ esu of cluster **7**] is roughly treated as β_{zzz}. The average $\chi_{zzz}^{(2)}(\omega)$ is estimated as large as 300×10^{-9} esu which is about 10 times larger than the second-order nonlinear optical coefficients of a traditional IR nonlinear optical crystal, $AgGaS_2$ ($d_{36}(AgGaS_2) \approx 11$ pm/V ($\approx 26 \times 10^{-9}$ esu) [8]).

3 Conclusions and Perspectives

In this minireview article, we provided the recent studies on the second-order NLO properties of dinuclear, trinuclear, and pentanuclear metal cluster compounds with the comprehensive discussions on the intrinsic second-order NLO mechanism.

There exist multiple electronic transition processes that collectively contribute to the quadratic hyperpolarizability including MLCT, LMCT, MMCT, and metal-inductive LLCT. The MMCT features the NLO response mechanism of these polynuclear clusters with direct metal–metal interactions. The multiple transition processes are either cooperative to each other, such as the MLCT and MMCT synergetically enhance the β value of dinuclear model **1**, or are destructively interfering with each other, such as LMCT and MMCT can make opposite contribution to the β value of dinuclear model **2**. The traditional two-level model seems no longer valid for the complex polynuclear metal clusters because multiple excited states are coupled to the ground state to contribute to the β. For a clear description, the global β value (β_{tot}) can be denoted by the summation of the fractional β values contributed by the various CT processes: $\beta_{\mathrm{tot}} = \beta_{\mathrm{MLCT}} + \beta_{\mathrm{LMCT}} + \beta_{\mathrm{MMCT}} + \beta_{\mathrm{LLCT}} + \ldots$. For example, for anionic cluster **3**, the global β value can be accordingly denoted by $\beta_{\mathrm{tot}}(\mathbf{3}) \propto |\beta_{\mathrm{MLCT}}| - |\beta_{\mathrm{LMCT}}| + |\beta_{\mathrm{MMCT}}|$ in the magnitude order. The relatively weaker Mo–Cu interaction in model **3** results in the smaller β_{MMCT} fraction in the global β value. On the other side, the relatively intense Mo–Mo interaction in model **4** corresponds to the relatively large β_{MMCT} value ($\beta_{\mathrm{MMCT}} \sim 0.2\beta_{\mathrm{tot}}$). The intense direct metal–metal bonding interactions would result in the greater β_{MMCT} fractions in the global β_{tot} values, e.g., for a dirhenium model **1** with Re≡Re triple bond, β_{MMCT} fraction is about three fifth of the β_{tot} value.

The direct metal-to-metal transition process has been unambiguously confirmed to be the one of the second-order response mechanisms of these metal cluster compounds. This unique MMCT process could positively enhance the quadratic hyperpolarizability, and in some cases, its contribution is significant. It provides one promising means to tune the second-order NLO effects of metal cluster compounds by adjusting the metal–metal interactions. In contrast to tune the size and degree of delocalized π-conjugated ligands and the strength of the molecular

dipole moments, this adjustment will less affect the IR absorptions, especially in the mid-IR region. As a result, the IR transparency (seriously depends on coordinate ligands) and nonlinearity (can rely on metal–metal bonding) can be separately tuned benefiting to the improvement of the transparency–nonlinearity trade-off. This understanding of the detailed relationship between the direct metal–metal interaction and second-order optical nonlinearity will open a way to the further investigation in the metal cluster compounds for the novel IR second-order NLO materials and the optical molecular devices.

References

1. Chai BHT (1995) Optical materials. In: Weber MJ (ed) CRC handbook of laser science and technology, vol 2. CRC, Boca Raton
2. Chemla DS (1971) Opt Commun 3:29
3. Boyd GD, Kasper H, McFee JH (1971) IEEE J QE-7:563
4. Shay LJ, Wernick JH (eds) (1975) Ternary chalcopyrite semiconductors. Growth, electronic properties and applications. Pergamon, New York
5. Schunemann PG (2006) Proc SPIE 6103:610303
6. Swain JE, Stokowski SE, Milam D, Kennedy GC (1982) Appl Phys Lett 41:12
7. Boyd GD, Buehler E, Storz FG (1971) Appl Phys Lett 18:301
8. Roberts DA (1992) IEEE J 28:2057
9. Mason PD, Jackson DJ, Gorton EK (1994) Opt Commun 110:163
10. Verozubova GA, Okunev AO, Gribenyukov AI, Trofimiv AYu, Trukhanov EM, Kolesnikov AV (2010) J Cryst Growth 312:1122
11. Byer RL, Choy MM, Herbst RL, Chemla DS, Feigelso RS (1974) Appl Phys Lett 24:65
12. Kildal H, Iseler GW (1976) Appl Opt 15:3062
13. Wu K, Chen C (1992) Appl Phys A54:209
14. Zhang G, Qin J, Liu T, Li Y, Wu Y, Chen C (2009) App Phys Lett 95:261104
15. Di Bella S (2001) Chem Soc Rev 30:355
16. Chemla DS, Zyss J (eds) (1987) Nonlinear optical properties of organic molecules and crystals. Academic, New York
17. Nalwa HS, Miyata S (eds) (1997) Nonlinear optics of organic molecules and polymers. CRC, New York
18. Marder SR, Gorman CB, Meyers F, Perry JW, Bourhill G, Bredas J-L, Pierce BM (1994) Science 265:632
19. Wolff JJ, Langle D, Hillenbrand D, Wortmann R, Matschiner R, Glania C, Kramer P (1997) Adv Mater 9:138
20. Lacroix PG, Malfant I, Iftime G, Razus AC, Nakatani K, Delaire JA (2000) Chem Eur J 6:2599
21. Brunel J, Ledoux I, Zyss J, Blanchard-Desce BM (2001) Chem Commun 923
22. Brunel J, Mongin O, Jutand A, Ledoux I, Zyss J, Blanchard-Desce M (2003) Chem Mater 15:4139
23. Goodson TG (2005) Acc Chem Res 38:99
24. Hennrich G, Murillo MT, Prados P, Al-Saraierh H, El-Dali A, Thompson DW, Collins J, Georghiou PE, Teshome A, Asselberghs I, Clays K (2007) Chem Eur J 13:7753

25. Frasier CC, Harvey MA, Cokerham MP, Hand HM, Chauchard EA, Lee CH (1986) J Phys Chem 90:5703
26. Green ML, Marder SR, Thompson ME, Bandy JA, Bloor D, Kolinsky PV, Jones RJ (1987) Nature 330:360
27. Nalwa HS (1991) Appl Organomet Chem 5:349
28. Tessore F, Roberto D, Ugo R, Quici PS, Ledoux-Rak I, Zyss J (2003) Angew Chem Int Ed 42:456
29. Powell CE, Humphery MG (2004) Coord Chem Rev 248:725
30. Cariati E, Pizzotti M, Roberto D, Tessore F, Ugo R (2006) Coord Chem Rev 250:1210
31. Coe BJ (2006) Acc Chem Res 39:383, and the references therein
32. Morrall JPL, Humphrey MG, Dalton GT, Cifuentes MP, Samoc M (2006) In: Padadopoulos MG, Sadlej AJ, Leszczynski J (eds) Nonlinear optical properties of matter, from molecules to condensed phases. Springer, Dordrecht, p 537, and the references therein
33. Senge MO, Fazekas M, Notaras EGA, Blau WJ, Zawadzka M, Locos OB, Ni Mhuircheartaigh EM (2007) Adv Mater 19:2737
34. Duncan TV, Song K, Hung S-T, Miloradovic I, Nayak A, Persoons A, Verbiest T, Therien MJ, Clays K (2008) Angew Chem Int Ed 47:2978
35. Kanis DR, Ratner MA, Marks TJ (1992) J Am Chem Soc 114:10338
36. Kanis DR, Lacroix PG, Ratner MA, Tobin JM (1994) J Am Chem Soc 116:10089
37. Matsuzawa N, Seto J, Dixon DA (1997) J Phys Chem A 101:9391
38. Karton A, Iron MA, van der Boom ME, Martin JML (2005) J Phys Chem A 109:5454
39. Asselberghs I, Therien MJ, Coe BJ, McCleverty JA, Clays K (2006) In: Schubert US, Newkome GR (eds) Metal-containing and metallosupramolecular polymers and materials. ACS symposium series, vol 928. American Chemical Society, Distributed by Oxford University Press, Washington, p 527
40. Coe BJ (2006) In: Padadopoulos MG, Sadlej AJ, Leszczynski J (eds) Nonlinear Optical Properties of Matter, From Molecules to Condensed Phases. Springer, Dordrecht, p 571, and the references therein
41. Sophy KB, Calaminici P, Pal S (2007) J Chem Theory Comput 3:716
42. Laidlaw WM, Denning RG, Verbiest T, Chauchard E, Persoons A (1993) Nature 363:58
43. Lin CS, Wu KC, Snijders JG, Sa RJ, Chen XH (2002) Acta Chim Sinica 60:664
44. de Angelis F, Fantacci S, Sgamelotti A, Cariati F, Roberto D, Tessore F, Ugo R (2006) Dalton Trans 852
45. Wu K (2006) In: Maroulis G (ed) Atoms, Molecules and Clusters in Electric Fields. Imperial College Press, London, p 565
46. Liao Y, Eichinger BE, Firestone KA, Haller M, Luo J, Kaminsky W, Benedict JB, Reid PJ, Jen AK-Y, Dalton LR, Robinson BH (2005) J Am Chem Soc 127:2758
47. Coe BJ, Harris JA, Brunschwig BS, Asselberghs I, Clays K, Garin JJ, Orduna J (2005) J Am Chem Soc 127:13399
48. Roberto D, Ugo R, Tessore F, Lucenti E, Quici S, Vezza S, Fantucci PC, Invernizzi I, Brum S, Ledoux-Rak I, Zyss J (2002) Organometallic 21:161
49. Senechal K, Maury O, Le Bozec H, Ledoux I, Zyss J (2002) J Am Chem Soc 124:4561
50. Rigamonti L, Demartin F, Forni A, Righetto S, Pasini A (2006) Inorg Chem 45:10976
51. Fukui H, Kishi R, Minami T, Nagai H, Takahashi H, Kubo T, Kamada K, Ohta K, Champagne B, Botek M, Masayoshi Nakano M (2008) J Phys Chem A 112:8423
52. Muller TJJ, Netz A, Ansorge M, Schmalzlin E, Brauchle C, Meerholz K (1999) Organometallic 18:5066
53. Roberto D, Ugo R, Bruni S, Cariati E, Cariati F, Fantucci PC, Invernizzi I, Quici S, Ledoux I, Zyss J (2000) Organometallic 19:1775
54. Maury O, Viau L, Senechal K, Corre B, Guegan JP, Renouard T, Ledoux I, Zyss J, Le Bozec H (2004) Chem Eur J 10:4454
55. Labat L, Lamere J-F, Sasaki I, Lacroix PG, Vendier L, Asselberghs I, Perez-Moreno J, Clays K (2006) Eur J Inorg Chem 3105

56. Nguyen P, Lesley G, Marder TB, Ledoux I, Zyss J (1997) Chem Mater 9:406
57. McDonagh AM, Humphrey MG, Samoc M, Luther-Davies B, Houbrechts S, Wada T, Sasabe H, Persoons A (1999) J Am Chem Soc 121:1405
58. Weyland T, Ledoux I, Brasselet S, Zyss J, Lapinte C (2000) Organometallic 19:5235
59. Pizzotti M, Ugo R, Dragonetti C, Annoni E (2003) Organometallic 22:4001
60. Wu K, Li J, Lin C (2004) Chem Phys Lett 388:353
61. Wu K, Sa R, Lin C (2005) New J Chem 29:362
62. Li Q, Sa R, Wei Y, Wu K (2008) J Phys Chem A 112:4965
63. Isaenko L, Yelisseyev A, Lobanov S, Petrov V, Rotermund F, Slekys G, Zondy JJ (2002) J Appl Phys 91:9475
64. Gradinaru J, Forni A, Druta V, Tessore F, Zecchin S, Quici S, Garbalau N (2007) Inorg Chem 46:884
65. Coe BJ, Jones LA, Harris JA, Brunschwig BS, Asselbergh I, Clays K, Persoons A, Garin J, Orduna J (2004) J Am Chem Soc 126:3880
66. Inerbaev TM, Belosludov RV, Mizuseki H, Takahashi M, Kawazoe Y (2006) J Chem Theory Comput 2:1325
67. Senechal-David K, Hemeryck A, Tancrez N, Toupet L, Williams JAG, Ledoux I, Zyss J, Boucekkine A, Guegan JP, Le Bozec H, Maury O (2006) J Am Chem Soc 128:12243
68. Champagne B, Perpete EA, van Gisbergen SJA, Baerends EJ, Snijders JG, Soubra-Ghaoui C, Robins KA, Kirtman B (1998) J Chem Phys 109:10489
69. van Gisbergen SJA, Schipper PRT, Gritsenko OV, Baerends EJ, Snijders JG, Champagne B, Kirtman B (1999) Phys Rev Lett 83:694
70. Jacquemin D, Andre JM, Perpete EA, Sekino H, Yasuyuki M, Kamiya M, Hirao K (2004) J Chem Phys 121:4389
71. Jacquemin D, Perpete EA, Ciofini I, Adamo C (2005) Chem Phys Lett 405:376
72. Champagne B, Perpete EA, Jacquemin D, van Gisbergen SJA, Baerends EJ, Soubra-Ghaoui C, Robins KA, Kirtman B (2000) J Phys Chem A 104:4755
73. Zhang M, Wu KC, Liu C, Wei Y (2005) Acta Phys Sinica 54:1762
74. Bruschi M, Fantucci P, Pizzotti M (2005) J Phys Chem A 109:9637
75. van Faassen M, de Boeij PL, van Leeuwen R, Berger JA, Snijders JG (2002) Phys Rev Lett 88:186401
76. Gonze X, Ghosez P, Godby RW (1995) Phys Rev Lett 74:4035
77. Champagne B, Bulat FA, Yang WT, Bonness S, Kirtman B (2006) J Chem Phys 125:194114
78. Bulat FA, Toro-Labbe A, Champagne B, Kirtman B, Yang WT (2005) J Chem Phys 123:014309
79. Sexton JZ, Kummel AC (2003) J Vacuum Sci Technol B 21:1908
80. Lee C, Yang W, Parr RG (1988) Phys Rev B 37:785
81. Becke AD (1993) J Chem Phys 98:5648
82. Adamo C, Barone V (1998) J Chem Phys 108:664
83. Perdew JP, Wang Y (1992) Phys Rev B 45:13244
84. Hieringer W, Baerends EJ (2006) J Phys Chem A 110:1014
85. Cotton FA, Extine MW (1978) J Am Chem Soc 100:3788
86. Cai S, Hoffman DM, Wierda DA (1991) Inorg Chem 30:827
87. Becke AD (1988) Phys Rev A 38:3098
88. Perdew JP (1988) Phys Rev B 33:8822
89. Ceperly DM, Alder BJ (1980) Phys Rev Lett 45:566
90. Vosko SH, Wilk L, Nusair M (1980) Can J Phys 58:1200
91. Stoll H, Pavlidou CME, Preuss H (1978) Theor Chim Acta 49:143
92. van Lenthe E, Baerends EJ, Snijders JG (1993) J Chem Phys 99:4597
93. van Lenthe E, Baerends EJ, Snijders JG (1996) J Chem Phys 105:6505
94. van Lenthe E, Ehlers AE, Baerends EJ (1999) J Chem Phys 110:8943
95. van Gisbergen SJA, Snijders JG, Baerends EJ (1998) J Chem Phys 109:10644

96. te Velde G, Bickelhaupt FM, Baerends EJ, Fonseca-Guerra C, van Gisbergen SJA, Snijders JG, Ziegler T (2001) J Comput Chem 22:931
97. Mayer I (1983) Chem Phys Lett 97:270
98. Barclay T, Eglin JL, Smith LT (2001) Polyhedron 20:767
99. Dequeant MQ, Bradley PM, Xu GL, Lutterman DA, Turro C, Ren T (2004) Inorg Chem 43:7887
100. Golichenko AA, Shtemenko AV (2006) Russ J Coord Chem 32:242
101. Landis CR, Weinhold F (2006) J Am Chem Soc 128:7335
102. Acott SR, Garner CD, Nicholson JR, Clegg W (1983) J Chem Soc Dalton Trans 713
103. Zhu NY, Zheng YF, Wu XT (1990) Inorg Chem 29:2705
104. Klamt A (1995) J Phys Chem 99:2224
105. Klamt A, Jones V (1996) J Chem Phys 105:9972
106. Pye CC, Ziegler T (1999) Theor Chem Acc 101:396
107. Klamt A, Schüürmann G (1993) J Chem Soc Perkin Trans 2 799
108. Clays K, Persoons A (1991) Phys Rev Lett 66:2980
109. Hendrickx E, Clays K, Persoons A (1998) Acc Chem Res 31:675, and the references therein
110. Oudar JL, Chemla DS (1977) J Chem Phys 66:2664
111. Cyvin SJ, Rauch JE, Decius JC (1965) J Chem Phys 43:4083
112. Bersohn R, Pao YH, Frisch HL (1996) J Chem Phys 45:3184
113. Pizzotti M, Ugo R, Roberto D, Bruni S (2002) Organometallic 21:5830
114. Zhang C, Song YL, Kuhn FE, Wang Y, Fun H, Xin XQ (2002) J Mater Chem 12:239
115. Zhang C, Song YL, Kuhn FE, Wang Y, Xin XQ, Herrmann WA (2002) Adv Mater 14:818
116. Zhang QF, Zhan Y, Ding JH, Song YL, Rothenberger A, Fenke D, Leung WH (2006) Inorg Chem 45:5148
117. Muller A, Bogge H, Schimanski U (1983) Inorg Chim Acta 69:5
118. Chemla DS, Oudar JL, Jerphagnon J (1975) Phys Rev B 12:4534